

MASTER'S THESIS REPORT
DEPARTMENT OF MECHANICAL ENGINEERING
UNIVERSITY WEST

EB-PBF additive manufacturing of Alloy 718

Effect of shot peening on surface characteristics and high temperature corrosion performance

Venkataramanan Mohandass



Acknowledgments

I sincerely thank my supervisor Dr. Esmail Sadeghi for his guidance and continuous support by reviewing my thesis work at every stage of completion. I thank University West and my home university for the opportunity to do my Master's thesis at PTC as a foreign exchange student from SRMIST. I express my gratitude to Kenneth Andersson and Björn Särnerblom for providing the training. I acknowledge other institutes and companies who helped me with conducting some of the experiments for my project. I finally thank all my friends and colleagues who helped in my thesis work. I wish everyone the best of luck.

Abstract

There is an upsurge of research interest on Alloy 718 additively manufactured (AM) by electron beam powder bed fusion (EB-PBF) technique in aero and land-based gas turbine engines. However, the surface quality of the manufactured components has always been a major challenge. Several factors, including powder particle size, layer thickness, beam parameters, scanning strategies, and inclination angle of the build, govern the surface characteristics. Along with surface roughness resulted from partially melted powder particles, surface defects such as balls, satellites, microcracks as well as up-skin and down-skin surfaces can enhance the vulnerability of the manufactured parts to corrosion. When the surface is unable to withstand the exposed environment adequately, corrosion can be triggered. The surface-induced corrosion failures are increasingly becoming more challenging as the AM components often have complex geometries that render them even more difficult to finish. So, the relatively poor surface finish is the barrier to the full exploitation of the AM industry.

In the present study, to achieve the desired surface quality, hence an improved high temperature corrosion performance, shot peening was implemented on Alloy 718 parts manufactured by EB-PBF. The high temperature corrosion behavior of the parts was investigated in an ambient air environment at 650 and 800 °C for up to 336 h. The underlying physical and chemical factors at play of the parts exposed to the corrosive environment were investigated too. The effect of topographical features (e.g., surface roughness) and microstructural characteristics (e.g., grain structure, phases, and defects) on high temperature corrosion behavior were analyzed by 3D surface profilometry, hardness test, optical microscopy (OM), scanning electron microscopy (SEM) equipped with energy disperse spectroscopy (EDS), X-ray diffractometry (XRD) and electron backscatter diffraction (EBSD). The surface roughness and high temperature corrosion rate of the parts was significantly reduced after shot peening.

Keywords: Alloy 718, Additive manufacturing, Electron beam-powder bed fusion, Surface engineering, Shot peening, High temperature corrosion

Table of Contents

ACKNOWLEDGEMENTS	II
ABSTRACT	III
TABLE OF CONTENTS	I
LIST OF FIGURES	I
1. INTRODUCTION.....	1
1.1. GAS TURBINE IN THE AEROSPACE INDUSTRY.....	1
1.2. BACKGROUND AND MOTIVATION	2
1.3. AIM.....	3
2. MATERIAL AND DEFECTS.....	4
2.1. ALLOY 718.....	4
2.2. MICROSTRUCTURE	4
2.3. DEFECTS.....	5
2.3.1. Porosity	5
2.3.2. Lack of fusion	6
2.3.3. Residual stress.....	7
2.3.4. Surface roughness	7
3. MANUFACTURING AND POST-TREATMENT.....	9
3.1. ADDITIVE MANUFACTURING PROCESS.....	9
3.2. POWDER BED FUSION.....	9
3.3. EB-PBF	9
3.4. SURFACE ENGINEERING TECHNIQUES TO REDUCE CORROSION	11
3.5. SHOT PEENING.....	11
3.6. HOT ISOSTATIC PRESSING + HEAT TREATMENT (HIP-HT).....	12
4. HIGH TEMPERATURE CORROSION (HTC)	14
4.1. OXIDE FORMATION AND CORROSION THEORY.....	14
4.2. THERMODYNAMICS AND KINETICS OF CORROSION.....	15
5. EXPERIMENTS	17
5.1. SAMPLE PREPARATION.....	17
5.2. POST-PROCESSING	18
5.2.1. Hot isostatic pressing + heat treatment (HIP-HT).....	18
5.2.2. Shot peening	19
5.3. OPTICAL MICROSCOPE, POROSITY MEASUREMENT	19
5.4. SCANNING ELECTRON MICROSCOPE (SEM)	20
5.4.1. Energy dispersive X-ray spectroscopy (EDS) for elemental analysis	21
5.4.2. X-ray diffractometry (XRD), Residual stress measurement.....	22
5.4.3. Electron backscatter diffraction (EBSD), Orientation and texture analysis	23
5.4.4. Line roughness measurement	24
5.4.5. Effect of post-processing	24
5.4.6. Grain size measurement.....	25
5.4.7. Niobium-rich phase content.....	27
5.5. IMAGEJ	29
5.6. WHITE LIGHT INTERFEROMETRY (WLI) FOR TOPOGRAPHICAL ANALYSIS.....	30

5.7.	HARDNESS MEASUREMENT BY VICKERS MICROHARDNESS (HV).....	32
5.8.	OXIDATION EXPOSURES	32
6.	RESULTS AND DISCUSSION	34
6.1.	MATERIAL CHARACTERIZATION.....	34
6.2.	GRAIN SIZE.....	34
6.3.	NIOBIUM-RICH PHASE CONTENT	35
6.4.	POROSITY.....	35
1.1.	ORIENTATION AND TEXTURE ANALYSIS	36
1.2.	TOPOGRAPHICAL STUDY.....	36
1.2.1.	Line roughness	39
1.2.2.	Surface roughness	40
1.3.	RESIDUAL STRESS.....	42
1.4.	HARDNESS.....	43
1.5.	CORROSION EXPOSURE RESULTS.....	44
1.5.1.	Oxide layer.....	44
1.5.2.	Weight gain	45
1.5.3.	Energy dispersive X-ray spectroscopy (EDS) analysis	48
1.5.4.	Elemental point analysis.....	53
7.	CONCLUSIONS	55
	REFERENCES.....	56

List of Figures

FIGURE 1.1: CROSS-SECTIONAL VIEW OF THE GAS TURBINE OF AN AIRCRAFT.	1
FIGURE 1.2: A CORRODED GAS TURBINE BLADE OF AN AIRCRAFT (LEFT) AND FORMED OXIDE LAYER (RIGHT).	2
FIGURE 2.1: SEM IMAGES SHOWING SPHERICAL AND SHRINKAGE PORES.	6
FIGURE 2.2: SEM IMAGE SHOWING THE LOF AND DELTA PHASE.	7
FIGURE 3.1: A SCHEMATIC OF AN EB-PBF MACHINE.	10
FIGURE 3.2: A SCHEMATIC SHOWING THE EFFECT OF SHOT PEENING ON THE SURFACE.	11
FIGURE 3.3: DIAGRAM SHOWING A UNIFORM APPLICATION OF PRESSURE NORMALLY IN ALL DIRECTIONS.	12
FIGURE 4.1: A SCHEMATIC DEPICTING THE FORMATION OF INTERNAL AND EXTERNAL OXIDE LAYERS.	14
FIGURE 4.2: THE ELLINGHAM DIAGRAM USED FOR THERMODYNAMICS EVALUATION OF CORROSION REACTIONS.	15
FIGURE 5.1: SAMPLE PREPARATION FOR SURFACE CHARACTERIZATION AND HIGH TEMPERATURE EXPOSURE.	17
FIGURE 5.2: VARIATIONS IN TEMPERATURE AND PRESSURE DURING HIP-HT CYCLE, QUINTUS TECHNOLOGIES. ...	18
FIGURE 5.3: OM MICROGRAPHS SHOWING POROSITY OF DIFFERENT SAMPLES.	19
FIGURE 5.4: SCHEMATIC DIAGRAM SHOWING DIFFERENT DETECTORS OF SEM.	20
FIGURE 5.5: EJECTION OF SE AND X-RAY EMISSION UPON EXCITATION.	22
FIGURE 5.6: CURVE SHOWING THE ELECTRON COUNTS FOR DIFFERENT ELEMENTS ACROSS DIFFERENT VOLTAGES.	22
FIGURE 5.7: EXPERIMENTAL SET-UP AND PRINCIPLE OF XRD.	23
FIGURE 5.8: IMAGE (LEFT) SHOWING THE EXPERIMENTAL SET-UP AND IMAGE (RIGHT) SHOWING DIFFERENT CRYSTALLOGRAPHIC ORIENTATIONS THAT CAN BE MEASURED.	24
FIGURE 5.9: SEM IMAGES (BSE MODE) SHOWING DIFFERENT ZONES (CONTOURS AND HATCH) FOR EACH SAMPLE.	25
FIGURE 5.10: IMAGE SHOWING THE GRAIN INTERSECTIONS ALONG A SERIES OF HORIZONTAL LINES.	26
FIGURE 5.11: SEM (BSE MODE) IMAGES SHOWING THE MICROSTRUCTURE OF PRE-EXPOSED SAMPLES.	26
FIGURE 5.12: SEM (BSE MODE) IMAGES SHOWING THE MICROSTRUCTURE OF EXPOSED SAMPLES AT 650°C AFTER 168 H.	26
FIGURE 5.13: SEM (BSE MODE) IMAGES SHOWING THE MICROSTRUCTURE OF EXPOSED SAMPLES AT 800 °C FOR 168 H.	27
FIGURE 5.14: SEM IMAGES (BSE MODE) SHOWING THE Nb-RICH ZONES OF THE PRE-EXPOSED SAMPLES.	28
FIGURE 5.15: SEM IMAGES (BSE MODE) SHOWING THE Nb-RICH ZONES OF THE EXPOSED SAMPLES AT 650 °C FOR 168 H.	28
FIGURE 5.16: SEM IMAGES (BSE MODE) SHOWING THE Nb-RICH ZONES OF THE EXPOSED SAMPLES AT 800 °C FOR 168 H.	29
FIGURE 5.17: HIGHLIGHTING POROSITY AND Nb-RICH ZONES USING IMAGEJ.	29
FIGURE 5.18: SCHEMATIC SHOWING THE WORKING PRINCIPLE OF WLI.	30
FIGURE 5.19: A DIAGRAM SHOWING THE INDENTER FOR MEASURING HV.	32
FIGURE 5.20: PICTURE OF THE SAMPLES BEFORE AND AFTER EXPOSURE FOR DIFFERENT TEMPERATURES AND DURATIONS.	33
FIGURE 6.1: RESULTS OF THE GRAIN SIZE MEASUREMENT.	34
FIGURE 6.2: RESULTS OF THE Nb-RICH ZONE MEASUREMENT.	35
FIGURE 6.3: RESULTS OF POROSITY MEASUREMENT.	36
FIGURE 6.4: EBSD ANALYSIS SHOWING GRAIN ORIENTATION AND TEXTURE FOR ALL THE SAMPLES IN THE CONTOUR REGION.	36
FIGURE 6.5: TOPOGRAPHICAL SEM IMAGES (SE MODE) OF THE SURFACE OF THE AS-BUILT SAMPLE UNDER DIFFERENT MAGNIFICATIONS.	37
FIGURE 6.6: TOPOGRAPHICAL SEM IMAGES (SE MODE) OF THE SURFACE OF THE SHOT PEENED SAMPLE UNDER DIFFERENT MAGNIFICATIONS.	38
FIGURE 6.7: TOPOGRAPHICAL SEM IMAGES (SE MODE) OF THE SURFACE OF THE HIP-HT SAMPLE UNDER DIFFERENT MAGNIFICATIONS.	38

FIGURE 6.8: TOPOGRAPHICAL SEM IMAGES (SE MODE) OF THE SURFACE OF THE HIP-HT + SHOT PEENED SAMPLE UNDER DIFFERENT MAGNIFICATIONS.	39
FIGURE 6.9: FIGURE SHOWING POINTS SELECTED FOR THE LINE ROUGHNESS MEASUREMENT AND PROFILE CURVES FOR A) AS-BUILT, B) SHOT PEENED, C) HIP-HT AND D) HIP-HT + SHOT PEENED SAMPLES.	40
FIGURE 6.10: LINE ROUGHNESS MEASUREMENT.	40
FIGURE 6.11: ENVELOPE THRESHOLD AND TOP VIEW.	41
FIGURE 6.12: SURFACE ROUGHNESS MAPPING.	41
FIGURE 6.13: SURFACE ROUGHNESS MEASUREMENT.	42
FIGURE 6.14: SCHEMATIC DEPICTING THE DIRECTION OF AXIAL AND HOOP STRESSES ALONG WITH THEIR CORRESPONDING MEASUREMENTS.	43
FIGURE 6.15: HARDNESS MEASUREMENT.	44
FIGURE 6.16: CHANGE IN HARDNESS WITH RESPECT TO THE DISTANCE FROM THE SURFACE.	44
FIGURE 6.17: TREND IN OXIDE GROWTH ACCORDING TO POST-PROCESSING.	45
FIGURE 6.18: OXIDE LAYER THICKNESSES FORMED ON THE SAMPLES WITH DIFFERENT POST-TREATMENT.	44
FIGURE 6.19: WEIGHT GAIN OF SAMPLE + CRUCIBLE FOR 96 H EXPOSURE TEST.	46
FIGURE 6.20: WEIGHT GAIN OF SAMPLE + CRUCIBLE FOR 168 H EXPOSURE TEST.	46
FIGURE 6.21: WEIGHT GAIN OF SAMPLE + CRUCIBLE FOR 336 H EXPOSURE TEST.	46
FIGURE 6.22: WEIGHT GAIN OF SAMPLE FOR 96 H EXPOSURE TEST.	47
FIGURE 6.23: WEIGHT GAIN OF SAMPLE FOR 168 H EXPOSURE TEST.	47
FIGURE 6.24: WEIGHT GAIN OF SAMPLE FOR 336 H EXPOSURE TEST.	47
FIGURE 6.25: TREND IN WEIGHT GAIN AT 650 °C.	48
FIGURE 6.26: TREND IN THE WEIGHT GAIN AT 800 °C.	48
FIGURE 6.27: SURFACE ELEMENTAL DISTRIBUTION FOR THE AS-BUILT SAMPLE.	49
FIGURE 6.28: SURFACE ELEMENTAL DISTRIBUTION FOR THE SHOT PEENED SAMPLE.	50
FIGURE 6.29: SURFACE ELEMENTAL DISTRIBUTION FOR THE HIP-HT SAMPLE.	50
FIGURE 6.30: SURFACE ELEMENTAL DISTRIBUTION FOR THE HIP-HT + SHOT PEENED SAMPLE.	51
FIGURE 6.31: LINE ELEMENTAL DISTRIBUTION FOR THE AS-BUILT SAMPLE.	51
FIGURE 6.32: LINE ELEMENTAL DISTRIBUTION FOR THE SHOT PEENED SAMPLE.	52
FIGURE 6.33: LINE ELEMENTAL DISTRIBUTION FOR THE HIP-HT SAMPLE.	52
FIGURE 6.34: LINE ELEMENTAL DISTRIBUTION FOR THE HIP-HT + SHOT PEENED SAMPLE.	53
FIGURE 6.35: VARIATION IN CONCENTRATIONS OF INDIVIDUAL ELEMENTS FOR ALL SAMPLES.	54

1. Introduction

1.1. Gas turbine in the aerospace industry

A series of blades placed at the front and rear with equidistant spacing (*see Figure 1.1*) lie within the hot and cold sections of the gas turbine, respectively. Atmospheric air is gushed into the compression chamber by the rotating action of front turbine blades, where the air is compressed by Venturi effect[1]. Upon compression, the high-pressure gases that are now at elevated temperature than ambient air, are forced into the combustion chamber where the fuel injectors spray the fuel. Upon combustion of the air by the fuel, there is a steep increase in temperature and pressure that are pushed onto the rear turbine blades and finally exit the system from the exhaust. Once these gases are exhausted, there is a sudden pressure drop across the system, which causes more air to be sucked into the compression chamber, thus propelling the system. As rear turbine blades are at the immediate vicinity to the combustion chamber and experience the highest temperatures and pressures of any other component in the turbine, they require complex construction of cooling channels. Additive manufacturing (AM) could be an efficient technology in the production of such parts.

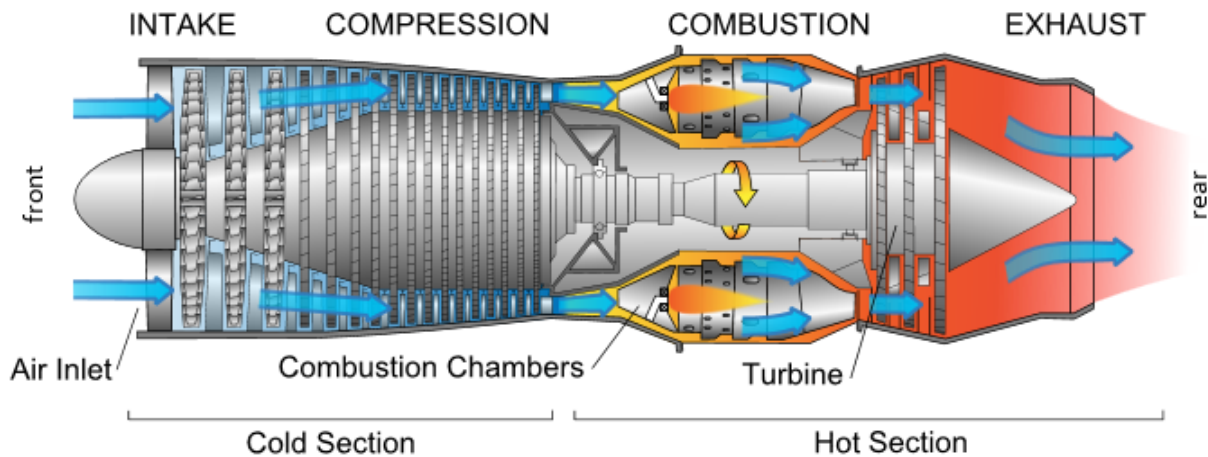


Figure 1.1: Cross-sectional view of the gas turbine of an aircraft.

Image courtesy: Jeff Dahl [2]

Consideration of corrosion-induced failure is of utmost importance in the aerospace industry to ensure its safety and life of operation [3]. Corrosion is a natural process that converts a metal (Me) to a more chemically stable form, such as its oxide (MeO), hydroxide (MeOH), or sulfide (MeS) [4]. It is the gradual destruction of materials (usually metals) by chemical and/or electrochemical reaction with their environment. Corrosion rate depends on temperature, pressure, post-

processing, and the concentration of the alloying elements that resist oxide layer formation. Corrosion, along with defects, can accelerate failure in the component.

1.2. Background and motivation

Art of producing entities in the required shape and size with desired material(s) according to the needs and application is called “manufacturing”[5]. Manufacturing has been evolved from conventional methodology to virtual prototyping and finally, rapid prototyping. Virtual prototyping had evolved after the era of modern computers, which utilizes a computer-aided design (CAD) model for simulations, discussions, and conclusions before deciding the final geometry and material for manufacturing. Advancement in science and technology lead to the evolution of rapid prototyping, interfacing computers with the manufacturing equipment. With the aid of this interface, by knowing the manufacturing constraints of the equipment, various parameters such as part orientation, and slicing, etc., of the CAD model can be varied to get the best possible output. Rapid prototyping, also called 3D printing, offers more choices in the design of the component with minimal manufacturing restrictions, saves time, cost, and work force[6]. Utilization of 3D printing technology enables the storage of the information regarding the manufacturing process as history, which has proven to be helpful for research and development. On the contrary, factors such as surface finish and high temperature corrosion (HTC) needs to be addressed in the AM industry. *Figure 1.2* shows the effect of HTC on the turbine blades.



Figure 1.2: A corroded gas turbine blade of an aircraft (left) and formed oxide layer (right).

Image courtesy: Shirsat U. M. [3]

Discussions within this paragraph are based on ideology extracted from [7][8][9][10]. Better surface characteristics can improve the service life of the turbine blades. A material is said to have a good surface integrity if it has no surface connected defects, high hardness, low surface roughness, low tensile residual stress, and high compressive residual stress. Surface characteristics can be improved by several post-processing techniques such as shot peening. Mechanical properties can be improved by post-treatment techniques such as isostatic pressing, and aging, etc. By having a good surface characteristic and mechanical strength, the material can withstand the harsh environment

experienced by a gas turbine engine for a longer duration. By knowing the effect of these post-processing and post-treatment technique(s) on the material in terms of strength, microstructure, and composition, manufacturing strategy for the component can be modified. Resources utilized for post-processing might be worthful considering the reduction in the frequency of maintenance as there are several steps involved in checking for errors and troubleshooting before the system gets going after the restart. Improving material properties also ensures the safety and reliability of the component.

1.3. Aim

Material science and engineering consist of four components[5] that are interdependent. These components for AM[6] are namely (i) processing parameters like air gap, bead size, raster width, and beam current, etc. (ii) microstructural properties like grain size, grain morphology, phases, and surface topology, etc. (iii) mechanical properties like ultimate tensile stress, fatigue strength, and yield strength, etc. (iv) performance characteristics such as corrosion resistance, shrinkage, and warpage, etc.

One major problem with EB-PBF is that it produces components with a rough surface finish [8]. Surface techniques such as shot peening, and machining, etc. are used to improve the surface integrity and mechanical strength of the manufactured parts, to improve its lifetime. Aim of this study is to know the effect of post processing techniques, in particular, shot peening, on surface integrity and corrosion resistance of the EB-PBF built parts.

2. Material and defects

2.1. Alloy 718

Alloy 718 is a Ni-Fe-based austenitic superalloy, which is highly suitable for working at elevated temperatures as they are corrosion resistant and possess strong mechanical properties. These properties make it more friendly with severe environments, both chemically and mechanically. They have a wide field of applications including gas turbine blades, spacers, and buckets in the high-speed airframe, rings, and castings in a liquid-fueled rocket, nuclear power plants, etc. The principal constituents of Alloy 718 are nickel followed by iron and chromium with the remaining as alloying elements. The strength and its capability to withstand high temperatures is achieved by strengthening mechanisms, namely solid solution hardening, precipitation hardening and grain size refinement. Constituents of Alloy 718 along with their compositions according to ASM standards are given below in *table 3.1*.

Table 2.1: Composition of Alloy 718 © ASM Aerospace Specification Metals Inc.

Element	Al	B	C	Co	Cr
wt %	0.2 – 0.8	0.006 max.	0.08 max.	1 max.	17 - 21
Element	Cu	Fe	Mn	Mo	Nb
wt %	0.3 max.	17	0.35 max.	2.8 – 3.3	4.75 – 5.5
Element	Ni	P	S	Si	Ti
wt %	50 – 55	0.015 max.	0.015 max.	0.35 max.	0.65 – 1.15

2.2. Microstructure

Alloy 718 possess a gamma matrix and face-centered cubic lattice structure at room temperature. However, when it is subjected to high temperature, the constituent element concentrations and grain morphology changes with time. Different phases of Alloy 718 in the order of precipitation with an increase in temperature, along with their corresponding lattice structure and solvus temperature during the evolution of microstructure is summarized by *S. William* as *Table 3.2* [11].

Niobium is the most important alloying element of Alloy 718 as it plays a crucial role in restoring the mechanical properties at high temperature. As a factor of which the strength of each phase depends upon Nb concentration apart from grain morphology. The degree of mismatch between the γ'' phase and γ -matrix are more than that between γ' and γ -matrix. Despite this reason, γ'' phase imparts more rigidity to the alloy than γ' phase, with γ'' and γ' phases forming the primary and secondary strengthening phases of Alloy 718 respectively. It is because of the transformation of the material from austenite to martensite in γ'' phase, thus having a supersaturation of carbon atoms. These C atoms form dislocations that impart kinetic hindrance to the grain growth, forming

a metastable γ'' phase. γ''/γ' ratio or the volume fraction is used to deduce the strength of the material, which depends upon (Al+Ni) /Nb ratio telling which of the two phases precipitates first. Intragranular δ needles form the strengthening phase by pinning at grain boundaries (see Figure 2.3) and being partially coherent with the γ -matrix. However, intragranular δ needles are detrimental as they are incoherent with the γ -matrix and cause distortion at the grain boundaries and soon begin to grow into the matrix forming globules. They also consume Nb by transforming γ'' into globular δ phase. Intergranular metal carbides (MC's) are strengthening whereas, intragranular MC's are detrimental, with the probability of forming a carbide in the matrix being more, this phase is less strengthening than δ phase. Laves phase is the most detrimental phase of Alloy 718 as it prevents dislocation motion and serves as crack initiation sites. From the formation of δ phase till laves, γ'' continues to grow, reaching a more than optimal size in laves phase, creating Nb depleted zones in the matrix. Following is the arrangement of phases in the order of increasing strengthening effect that has been summarized based on discussions by *Sames* [11]: Laves- $\text{Fe}_2(\text{Nb}, \text{Ti}, \text{Mo}) < \text{MC-NbC} < \delta\text{-Ni}_3\text{Nb} < \gamma'\text{-Ni}_3(\text{Al}, \text{Ti}) < \gamma''\text{-Ni}_3\text{Nb}$.

Table 2.2: Different phases of Alloy 718 along with their lattice structure and solvus temperature, *W. James* [11]

Phase	Crystal structure	Solvus temperature (°C)
γ	FCC	1227 – 1320
γ'	FCC	850 – 910
γ''	BCT	910 – 940
δ	Orthorhombic	1020
MC	Cubic	1260 - 1305
Laves	Hexagonal	1163

As mentioned before, morphology, size, and orientation of the grains also influence the strength of the matrix. Following is the evolution of grain morphology with the increase in temperature, summarized from *P. Karimi*. As the degree of mismatch increases between the γ and γ' phases, the γ' grains take up the following shapes, namely spherical, followed by globular, bulky and cuboidal with highest lattice mismatch. Whereas, γ'' always has a disk shape irrespective of change in lattice mismatch between γ and γ'' phases. Formation of δ needles and δ globules have already been discussed. Metallic carbides take up cubical grain morphology, and laves phase has an irregular globular structure or elongated platelets[12]. Another strength influencing factor is the grain size. *Hall E.* and *Petch N.* reported that decrease in grain size increases yield strength[13] [14]. *Ralston K.* also reported that finer grains have higher corrosion resistance[15]. *P. Karimi* reported that a {001} grain orientation showed the highest δ pinning at the grain boundaries[16].

2.3. Defects

2.3.1. Porosity

Porosity plays a vital role in the densification factor of the material during manufacturing. The strength of the material depends upon the percentage of porosity by area and its position, i.e., the quantity of presence in the surface and the bulk. Some of the errors that can occur during the

powder production are insufficient time interval for cooling down, fluctuations in temperature, improper vacuum, etc. These factors can lead to the entrapment of gas molecules within powder particles of the material, which, when used as the feed material for AM, it lowers the strength of the material. Pores are persistent even if all the process parameters fall in par with the ideal conditions as these are gas-induced porosity that is spherical (see Figure 2.1) in shape called as spherical porosity [17][12].

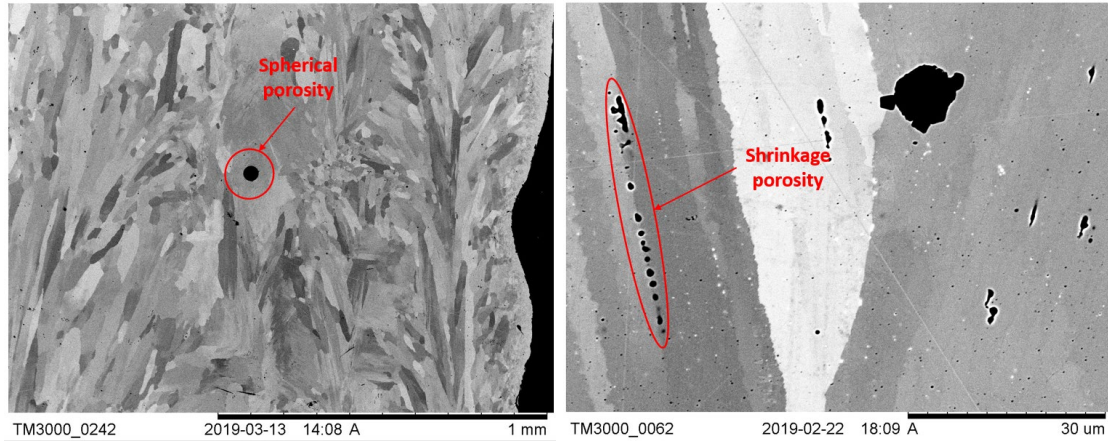


Figure 2.1: SEM images showing spherical and shrinkage pores.

The density of the material in its molten state is lesser than in its solid state. The material present at the surface usually has a higher cooling rate compared to the bulk material due to the heat transfer between the system and the surrounding. Because of this, material first starts to solidify at the surface and gradually traversing to the bulk, with however lower solidification rate. This time delay causes the surface to shrink compared to the bulk, which leads to the formation of an array of small pores placed quite close to each other called shrinkage porosity. When there is an increase in stress concentration, the location with shrinkage porosities is most prone to serve as crack initiation sites. *Strondl, A.* [18] stated that shrinkage porosity is the incomplete flow of metal into the desired melt region.

2.3.2. Lack of fusion

Whenever a certain region of the material is supplied with enough power (beam current), it causes that region to solidify completely before other surrounding regions. Due to this, while a new layer of material is extruded on top of the old layer, all the other parts of the material in the old layer fuses with the new layer leaving behind the unfused region. This unfused region creates pores in a highly disoriented shapes with different sizes, called the lack of fusion (LOF), which is a process-induced porosity [17][18].

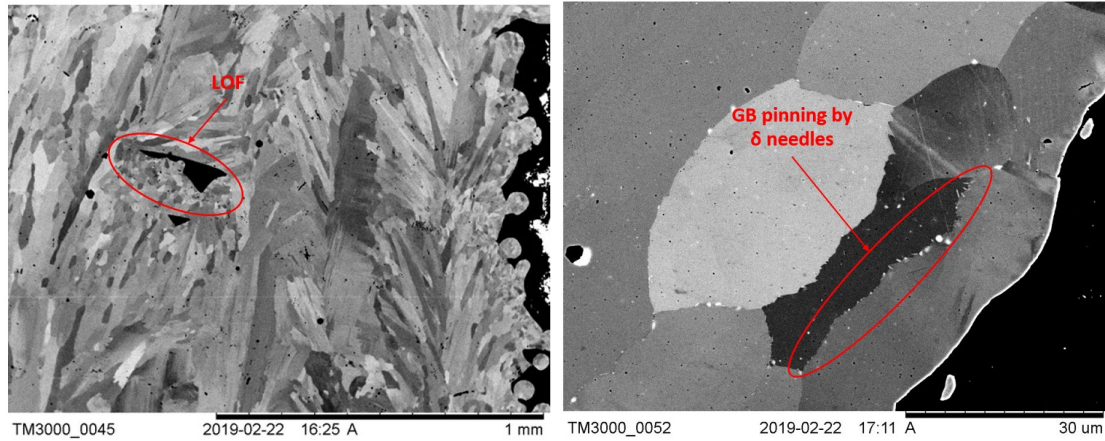


Figure 2.2: SEM image showing the LOF and delta phase.

LOF is possible not only during non-homogenous solidification but also when some regions get vaporized due to the striking of the beam with more than optimal power on the work material, as there is no material left out in that region for fusion. This type of defect is classified as a keyhole defect (see Figure 2.2). When there is an insufficient overlap between the adjacent melt pools, there is a shallow penetration of one layer into the other causing macroscale porosity, which is a quite large area with lack of fusion defect [17].

2.3.3. Residual stress

Residual stresses are those stresses, which reside in the material even after the removal of externally applied stresses. This occurs due to a sudden change in temperature of the material, called thermal shocks. Whenever there is a stack up of one layer over the other, during the process of fusion of the adjacent layers, there exist a thermal flux that induces internal stresses. When these stresses exceed the local yield stress value, it leads to the formation of cracks.

The feedstock material that is heated in the extrusion chamber, upon deposition tries to expand even after the interaction with the atmosphere. However, due to relatively lower ambient temperature, the molten material is restricted for further expansion, inducing compressive residual stresses. Once all the layers of the material have been extruded completely, then the material begins to shrink because of a gradual reduction in ambient temperature to near room temperature. This leads to the formation of tensile residual stresses, which are balanced out by the previously formed compressive stresses [19].

2.3.4. Surface roughness

Surface texture is the geometrical irregularities present at the surface that does not include those contributing to the shape of the surface. Surface texture is the form of a series of peaks and valleys that vary in height and spacing that are influenced by the method of manufacturing. Surface roughness is a component of surface texture that quantizes the height of these peaks and valleys. Topographies of the generated surfaces influence the accuracy and precision of the measurement of material properties which depend on the particle size, geometry, processes, etc. Townsend A. [20]

reported that components manufactured by the PBF techniques have frequent discontinuities, vertical walls, and re-entrant features.

3. Manufacturing and post-treatment

3.1. Additive manufacturing process

AM industry uses various technologies and methods for different applications to have a highly tailor-made microstructure, physical and chemical properties apart from custom geometry that best adheres to the requirements. There are three preliminary classifications of additive manufacturing (AM) based on their raw material, namely, liquid-based AM, solid-based AM, and powder-based AM [6]. They are further classified based on how the raw materials are solidified namely, powder bed fusion, direct energy deposition (DED), binder jetting, and sheet lamination. In this study, the AM process of interest is powder bed fusion (PBF), which can have either a laser (L) or an electron beam (EB) as the source for selective solidification, of which EB is chosen.

3.2. Powder bed fusion

In this type of AM process, the powder is spread on the entire layer, and only the required regions of that layer are solidified according to the cross section of the geometry, using a power source that can be either laser or an electron beam. The remaining unsintered powder is removed from the build chamber and is fed back into the reservoir for re-use until a certain number of times. The movement of powder is governed by the two delivery systems, namely the feed system and the build system that move towards and away from the build stage, respectively[21]. Rollers or rakes are used to level the sintered powder after the completion of every build layer, and this leveling is done before the movement of the build system and after the movement of the feed system. The powder surrounding the solidified powder with close compaction acts as a support structure during its solidification and helps eliminate bulging and deformations[21]. The powder for solidification is the build material, and those surrounding the build material is the build substrate. Usually, the build substrates are removed by a blast of air without using any external physical force. These substrates can be recycled until a limited number of cycles. However, depending on the build material characteristic, the build substrate can become more challenging for removal. More the difficulty in removal of build substrate more attention needs to be paid to take care of the features, not leading to undercuts or overhangs.

3.3. EB-PBF

When a certain potential difference is present across the filament, a large quantity of electrons, so-called "electron cloud" accumulates due to high electrical resistance [21]. Transportation of electrons from the cloud to the required location on the powder bed is governed by three pairs of lenses, namely astigmatism, focus, and deflection lenses (*see Figure 3.1*). This electron cloud when interacted with oppositely charged anodes, which has a higher potential difference than the cathode, called the astigmatism lens, accelerates the electrons from the cloud to the process chamber by attraction. Electrons already repelling each other, further widens because of attraction, thus falling apart from the collimated field. This lens is referred to as astigmatism, as it widens the

field view creating a shift in its trajectory. Upon acceleration, these electrons tend to deviate from its pathway due to high velocity, which is focused with the help of focus lenses. These focus lenses are the external magnetic coils, which when interacted by a beam of electrons creates an electromagnetic flux, that de-magnifies the beam to the desired spot size by varying the current across the magnetic coil. Smaller the spot size, higher is the concentration of electrons. Finally, the electron beam passes through the deflection lens that directs the electron to the required spot on the workpiece. Current in either of the two deflection lenses is adjusted to direct the beam, unlike the focus lenses in which current is varied equally. The powder is fed using a hopper on either side, and a rake is used to spread the powder evenly across the build platform, which when selectively solidified by the electron beam, is lowered for the process to repeat for the next layer. Last part that is generated after the deposition of all the layers of the geometry is termed as 'as-built' component that does not involve any post-processing.

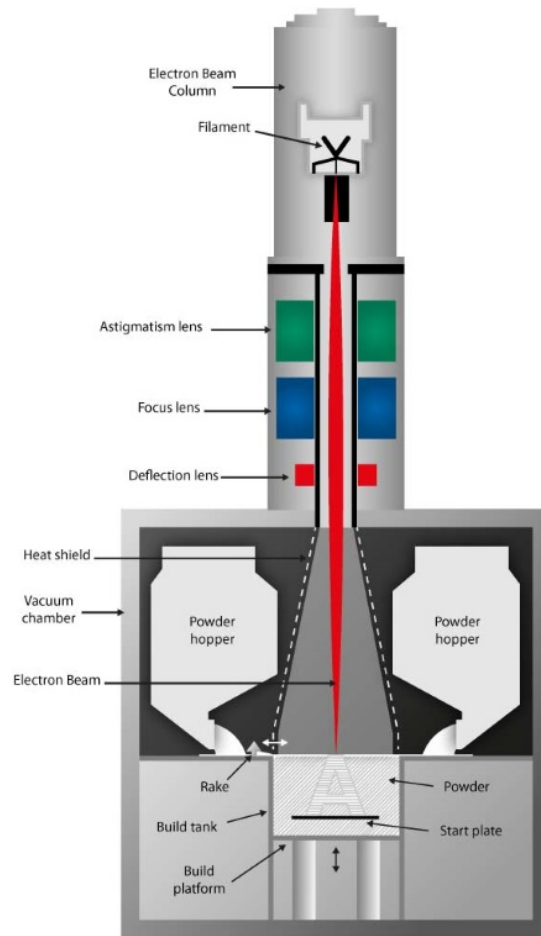


Figure 3.1: A schematic of an EB-PBF machine.

Image courtesy: Arcam EBM

Electron beam selectively melts and solidifies the powder on the bed firstly along the contour region, followed by the hatch region. EB-PBF employs spot melting, forming beads along the contours to have better precision and control, whereas a continuous back and forth movement of the beam forming the hatch region. All the three regions overlap each other and are governed by

several process parameters, including part orientation, raster angle, road width, air gap, and layer thickness, etc. [12].

3.4. Surface engineering techniques to reduce corrosion

Based on the discussions by *Uran, S.* [7], materials with smoother surface finish have higher residual stresses, a thin and uniform oxide layer, and much lesser iron concentrations in the oxide layer meaning lower nucleation sites to form metal oxides. *Pradban* reported that the rough surfaces have more tendency to get attacked by corrosion and have larger metal deficient regions than a smoother surface for Alloy 718 [8]. Due to these facts, it is important for a component to have a good surface finish for working at high temperatures for a long duration.

Some of the major approaches for providing good surface characteristics are as follows[1]: (i) polishing, grit blasting, electrochemical milling, and machining have no change in both microstructure and composition at the surface, (ii) shot peening, surface laser melting, and surface heat treatment changes the microstructure alone at the surface, (iii) diffusion coating and chromizing that change only the material composition at the surface, and (iv) applying an extra layer of HVAF thermal sprayed coating.

3.5. Shot peening

Shot peening is performed by the continuous bombardment of millions of tiny beads that flow through the nozzle at very high velocities on to the sample. As there is no force transmission into the bulk of the material due to a fractional impact duration, the microstructure is affected only at the surface (*see Figure 3.2*) with the phase composition being untouched throughout the material. Impact force, nozzle position, and sample position can be varied during the process.

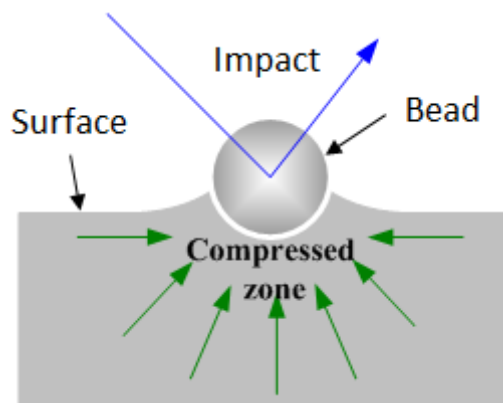


Figure 3.2: A schematic showing the effect of shot peening on the surface.

Image courtesy: Dmitri Kopeliovich, Substances and Technologies

Aeronautical components have tensile residual stresses as the applied stress is more than its nominal stress during operation, that can affect the service life due to a reduction in fatigue strength [8], [9]. *Zaleski K.* stated that compressive stresses are induced on the surface as a result of shot peening, increasing the fatigue life of Alloy 718 [22]. *Sanz, C.* reported that shot peening evenly distributes the residual stresses on the surface with a high magnitude of compressive residual stresses [9], [10]. *Zaleski K.* also reported that shot peened components apart from good surface

finish also has high roughness symmetricity [22]. Sanz, C. also reported that there is an increase in hardness, as well as porosity after shot peening on heat, treated Alloy 718 sample [9], [10]. However, the stand-alone influence of shot peening and heat treatment was not reported. Improved hardness is constructive, whereas the same with porosity is not. This increase in porosity can be due to heat treatment [23]. It has been reported by Damon J. that there is a substantial decrease in pore size when they are present near the surface compared to those away from the surface [24]. It shows that the surface porosity or open pores have a great positive impact on shot peening. Shot peening thus reduces surface roughness, minimizes surface connected defects, which is very helpful as hot isostatic pressing only reduces bulk defects, and imparts compressive residual stress and increases hardness to improve fatigue strength. Influence of shot peening on the surface characteristics depends upon working time, bead material, the distance between the source of impact and the sample, the distance between two consecutive points of impact on the sample, and impact energy [25].

3.6. Hot isostatic pressing + heat treatment (HIP-HT)

HIP is performed to eliminate closed pores inside the bulk, and HT is performed to strengthen the material by designing its microstructure. HT involves homogenization, followed by solutionizing and aging. Homogenization is the process of heating above the solvus temperature of a phase for dissolving it, and solutionizing is the process of heating just below the solvus temperature of a phase for re-precipitation. Solutionizing is performed after homogenization, which if not done properly then, the interdendritic region could be formed during solidification affecting the properties of microstructure [11]. However, each phase in the material has different solvus temperatures, as mentioned before. Aging is the process of introducing new grains with low dislocation densities by enhanced diffusion over long process hold temperatures to have good creep resistance.

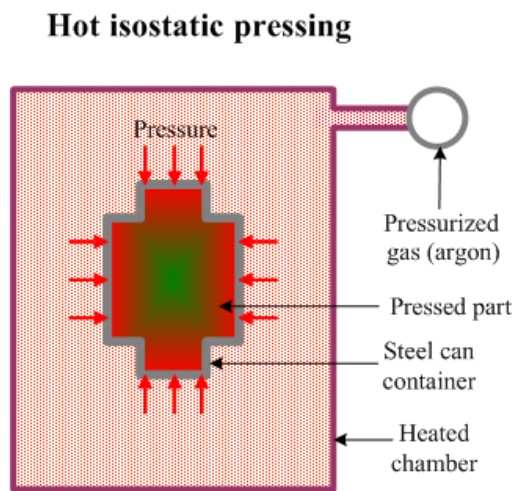


Figure 3.3: Diagram showing a uniform application of pressure normally in all directions.

Image courtesy: Dmitri Kopeliovich, Substances and Technologies

HIP is performed by applying pressure laterally inward, equally in all the directions perpendicular to the geometry (see Figure 3.3) using heated gases within a pressure vessel. Unlike unidirectional pressing, there is no friction involved, which causes re-distribution of forces causing different magnitudes of applied pressure at different locations. By having equal pressure distribution, the

geometry of the material is restored completely. During HIP, the yield strength of the material decreases, causing an increase in stresses that collapse the internal pores and lack of fusions, however leaving the surface connected defects untouched. Cracks present in bulk are also healed completely with no traces of existence just like other defects. Whereas, the surface cracks are not propagated further, as the forces present on the surface of the cracks are compensated by the presence of forces of required magnitude on the material surface in corresponding opposite directions. A dense gas with good thermal conductivity is used for pressing, as it facilitates good heat exchange between the heat source and the material, leading to the homogeneous temperature distribution. It can be seen from *Figure 5.2* that the temperature at the top and bottom of the furnace overlap throughout the cycle of operation. By eliminating internal porosity and other closed defects, the component reduces in size without any changes in geometry. Material shrinkage volume depends upon the densification percentage, number, and homogeneity of pores. Benefits of HIP include the elimination of stress concentration, which reduced stress intensity factor drastically, thus also tremendously reducing the probability of forming crack initiation sites. HIP also improves fatigue life, ductility, and fracture toughness, also making the material isotropic and more corrosion resistant.

HT is performed to strengthen the material further and most importantly, have desired material properties by controlling its microstructure. Tammas-Williams S [23], reported that there is regrowth in pores upon heat treatment. HIP sample still has porosity, but on a negligible scale, with entrapment of gas molecules used for HIP, which tends to expand upon a rise in temperature contributing to pore growth. These pores are still much smaller in size compared to the pre-worked condition, which further has a fractional increase in size for a very long duration at a constant temperature. However, there is no lack of fusion observed as they are completely healed.

4. High temperature corrosion (HTC)

4.1. Oxide formation and corrosion theory

At high operating temperature, oxygen (sourced from ambient air environment) is bonded to different elements on the surface of the material to form metallic oxides along with a single oxygen atom as a byproduct. However, the adhesion of oxygen on the surface does not get it dissolved into the bulk of the material. These oxygen atoms attract further atmospheric oxygen for stabilization, as they are more stable in their combined form rather than existing as a single entity, leading to the creation of oxygen nucleation sites. Upon longer process hold temperature, more and more oxygen is bonded with the metal atoms along with free oxygen atoms, causing the oxygen nucleation site to grow laterally along both sides. Growth of nucleation sites finally leads to the development of a thin sheet of an oxide layer on the surface of the material, followed by the inward dissolution of oxygen[26]. This oxide layer grows in time according to the temperature and alloy properties.

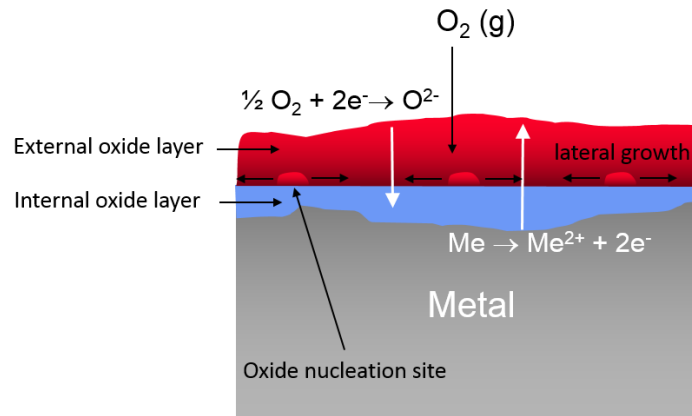


Figure 4.1: A schematic depicting the formation of internal and external oxide layers.

Image courtesy: Jeff Dahl [2]

An oxide layer that is formed (see Figure 4.1) at the surface of a material due to the interaction between the positively charged metal ions (Me^{2+}) and the negatively charged oxygen ions (O^{2-}) to form metal oxides (MeO) on the surface. High operating temperatures introduce lattice defects that changes the concentration of various alloying elements at different sites in the material. Whenever there is a change in concentration of any element, metal atoms within the material tends to diffuse from a region of higher concentration to a region of lower concentration, creating ionic imbalance. It causes the oxygen atom to move from the ambient air into the material (inward diffusion) and the metal atoms to move from the bulk towards the surface (outward diffusion). Homogeneity of the material is reduced while there is a displacement of a large number of metal atoms from the bulk, which affects the strength of the material. This oxide layer is characterized as a protective coating by a few aspects, which prevents the material below this layer from being further oxidized. An oxide layer is protective if it is thin, uniform, slow growing, adherent, and has a low vapor pressure and high melting point [4]. The extent of the protective nature of the oxide

layer depends upon the partial pressure and passivity of oxygen, and the amount of vaporization of chromium from the material.

4.2. Thermodynamics and kinetics of corrosion

According to the thermodynamics of HTC, there is a race (*see Figure 4.1*) between the inward diffusion of oxygen anions and the outward diffusion of metal cations [4]. Gibb's free energy at ground state, which can be determined from the Ellingham's diagram for the given temperature, shows the spontaneity of a reaction. Higher the Gibb's energy more is the spontaneity of the redox reaction to achieve equilibrium, thereby stabilizing the material-atmosphere interface, slowing down the oxide layer growth. Thermodynamics between metal and oxygen at high temperature also influences the direction of oxide layer growth, whether inward or outward. If the product of concentration and diffusivity of oxygen ions is more than that of metal ions, then the material forms an internal oxide layer, if not external oxide layer [4]. Thus, apart from the ionic concentration and of metal and oxygen atoms, the diffusion flux created at the interface and oxygen solubility also influences the direction of oxide layer growth. Inward oxide layer growth, upon the densification of metal oxides, gravity favors the growth internally unlike that for the external layer. On the other hand, external oxide layer growth causes more migration of metal atoms from the bulk, altering the dislocation densities present in the material. It can be seen from the Ellingham's diagram (*see Figure 4.2*) that Cr has the highest stabilizing effect among the ternary elements of Alloy 718. It has also been reported by Guan, S. W. that the solubility of oxygen reduces with an increase in Cr concentration [27]. It proves the importance of Cr in forming a protective oxide layer, and thus, Cr vaporization should be minimal.

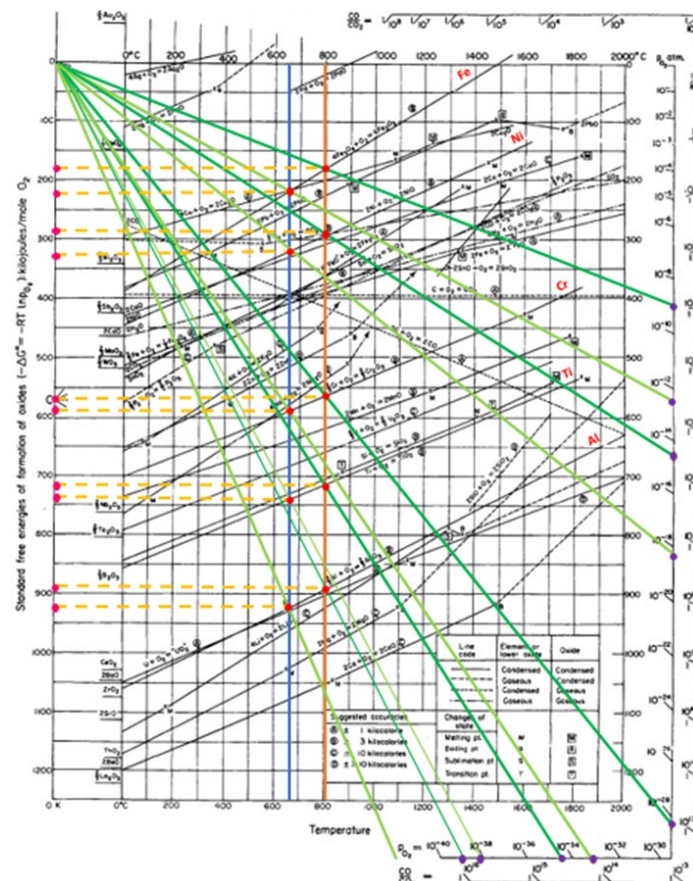


Figure 4.2: The Ellingham diagram used for thermodynamics evaluation of corrosion reactions. Image courtesy: web.mit.edu

Kinetics of corrosion is characterized by the trend in weight gain due to exposure with respect to time. The kinetics of oxide growth can be characterized by three trends, namely, logarithmic, linear, and parabolic. Following are the brief description of the trends:

In logarithmic growth, the electron movement is quite rapid at the beginning and subsidizes gradually over time, whereas, it continuously reduces with time in parabolic growth. Increasing oxide layer thickness creates porosity and the development of microcracks [26]. The rate of transportation of ions is directly proportional to time in linear growth. *Khanna, A. S.* concluded that the rate of oxidation decreases with an increase in oxide layer thickness [28]. *D. Young* inferred that, thinner the oxide layer the more protective it is [4]. Based on the theories drawn from [4], [26], and [28], the oxide growth trend can be summarized by arranging them in the order of decreasing protective nature as linear < logarithmic < parabolic.

5. Experiments

5.1. Sample preparation

A rod with a diameter of 20 mm and a height of 80 mm was cut into eight equal disks/samples. The same procedure was carried out for 4 rods, with each rod having different post-processing. A sample was used for characterization, and five samples were used for corrosion exposures (96, 168, 336 h at 650 and 800 °C). Position of the samples and slicing of the rods are marked along with the samples for the intended use (*see Figure 5.1*).

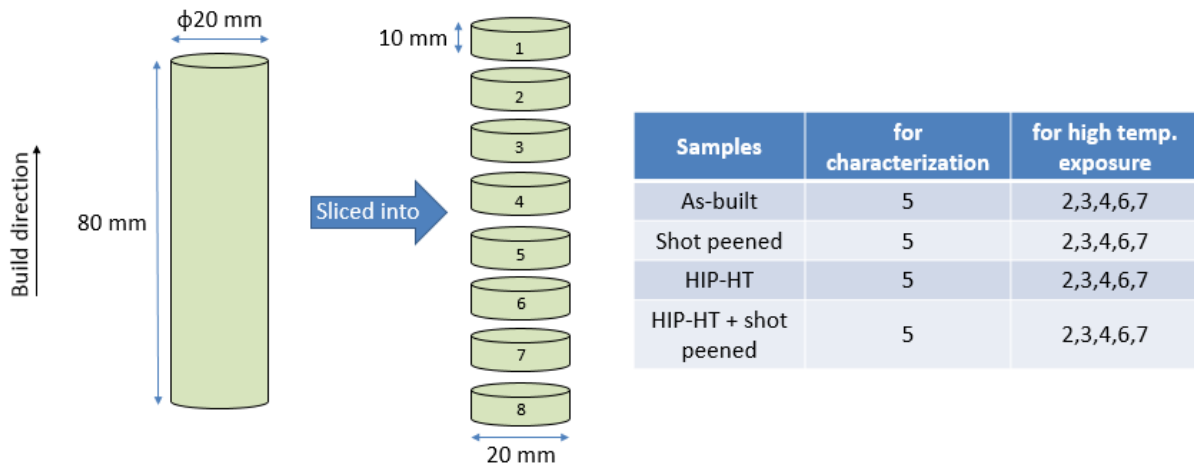


Figure 5.1: Sample preparation for surface characterization and high temperature exposure.

Pre-exposed samples were cut at a feed rate of 0.1 mm/s with a wheel speed of 2500 rpm using coolant, whereas the exposed samples were cut at a feed rate of 0.005 mm/s with a wheel speed of 300 rpm and without using coolant. The 96 and 336-hour exposed samples were used only to see the trend in weight gain and did not need any polishing or surface preparation. Apart from these, other 12 samples had prepared for viewing under SEM. 4 samples for surface characterization were hot mounted, grinded and polished by the following steps: 128, 75 and 45 μm for 2 min, 9 and 3 μm for 10 min and 0.05 μm for 15 min with a load of 25 KN. Other 8 samples after exposure were cold mounted, grinded and polished by the following steps: 75 and 45 μm for 2 min, 9 and 3 μm for 5 min and 0.05 μm with a load of 15 KN. Cold mounted samples are pressed against the grinding/polishing disc with a lower load than hot mounting due to their fragility. It had to be ensured that the oxide layer stayed intact with the sample after exposure for observation. The equipment used for cutting was Struers, grinding, and polishing was Buehler. 336-hour exposure at 650 °C (planned for sample 1) could not be carried out due to a technical difficulty. Sample 8 was not selected as the bottommost region of the rod experiences heat for the longest duration. Sample 5 was chosen for characterization as it has the neutral thermal effects compared to other

samples, for which sample 4 is also equally good. All the samples were manufactured in an A2X *Arcam machine* (Arcam EBM, Mölndal, Sweden) using Arcam standard process parameters.

5.2. Post-processing

5.2.1. Hot isostatic pressing + heat treatment (HIP-HT)

HIP and HT is combined in a single step by *Quintus Technologies, Sweden*, termed as HIP-HT, that saves energy, cost and increases productivity compared to single steps of HT and HIP. HIP-HT of the EB-PBF Alloy 718 samples for this study was carried out by *Quintus Technologies, Sweden*. By HIP-HT technique, the samples are not heated and cooled twice, rather just once, also that both HIP and HT can be done in the same furnace. The furnace consists of a unique cooling system that can undergo rapid cooling while withstanding high pressure, which reduces tension and improves fatigue life. Duration for homogenization, precipitation, aging, and quenching, along with total cycle time and pressure variations are provided in *Figure 5.2*, that is briefly discussed in the next paragraph. HIP and HT techniques are introduced in *section 3.3*.

HIP unit	QIH21	Date of execution	
Furnace	URC	Max Pressure	100,1773 Mpa
Operator		Max Temperature	1205 C°
Pressure media	Argon 4.8	Total cyclen time	24h

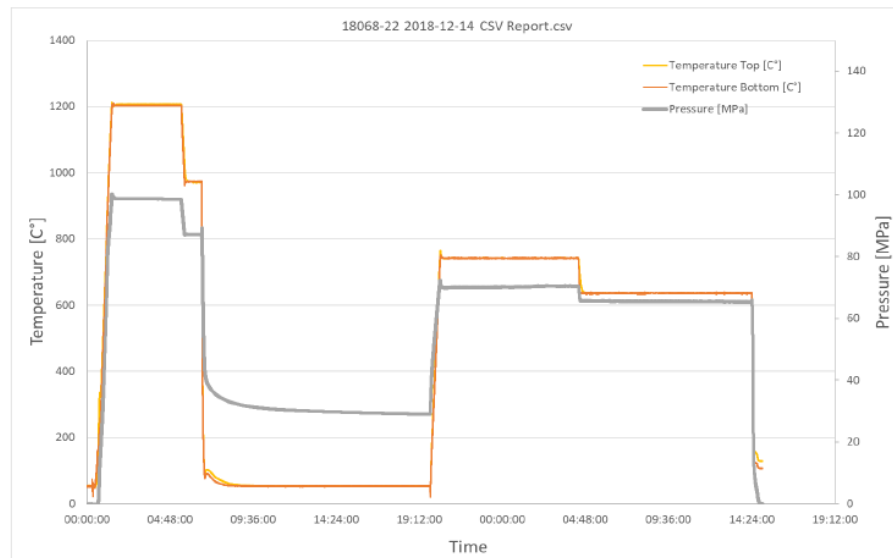


Figure 5.2: Variations in temperature and pressure during HIP-HT cycle, Quintus Technologies.

Temperature is ramped up to 1205 °C which is the homogenization temperature, that is slightly below the melting temperature of γ -matrix but higher than other phases except for MC's, where the material is at a transition state between solid and molten, which is perfect for isostatic pressing. At this temperature, the entire matrix is reset, however leaving behind traces of MC's. It is followed by the precipitation temperature close to 1000 °C, which is carefully chosen in a way to selectively precipitate only the δ needles and not the δ globules. After this, the material is quenched to near room temperature with a relatively small drop in pressure and holding for a while under high pressure. Next, the temperature is again ramped up to nearly 800 °C for precipitation of γ'' and γ' ,

after which it is dropped down for aging, followed by quenching to room temperature. The time duration and temperature for aging are carefully selected to have the required volume fraction γ''/γ' .

5.2.2. Shot peening

The surface of the samples was shot peened by glass beads (i.e., media blasting) using compressed air at ~ 380 KPa for 30 s. The bead diameter was between 70 and 140 μm . This treatment produced a clean, bright, smooth surface finish without dimensional change or contamination of the parts. The shot peening was carried out by *Curtis-Wright Surface Technologies (CWST)*.

5.3. Optical microscope, Porosity measurement

Images for porosity was taken in 10X magnification using *Zeiss Metal OM* shown in *Figure 5.3*. An optical microscope (OM) uses a light source for viewing the sample. Light rays that are emitted by the source hits the sample and are reflected, forming a magnified, inverted real image by the objective lens. This is further enlarged by the eyepiece to form a virtual image, which is fed to the computer digitally. Position of the sample, brightness, and contrast except focus can all be digitally controlled from the computer. The major advantage of this instrument is the fast acquisition of the sample's cross-section for a required magnification. This is done by automatically taking the required number of images, adjusting the focus points, overlapping and finally stitching them within the concise boundary limit specified by the user by setting start and end points on either corner of the sample. Apart from this, the degree of overlap and position of focus points can also be individually adjusted and varied by the user. By setting a different combination of brightness and contrast, depending upon the interest either the grain boundaries or pores can be viewed. Etching was not carried out for the samples as it favors the identification of grain boundaries but diminishes the visibility of pores. Quantization of these pores was done using a software called ImageJ, which is discussed later.

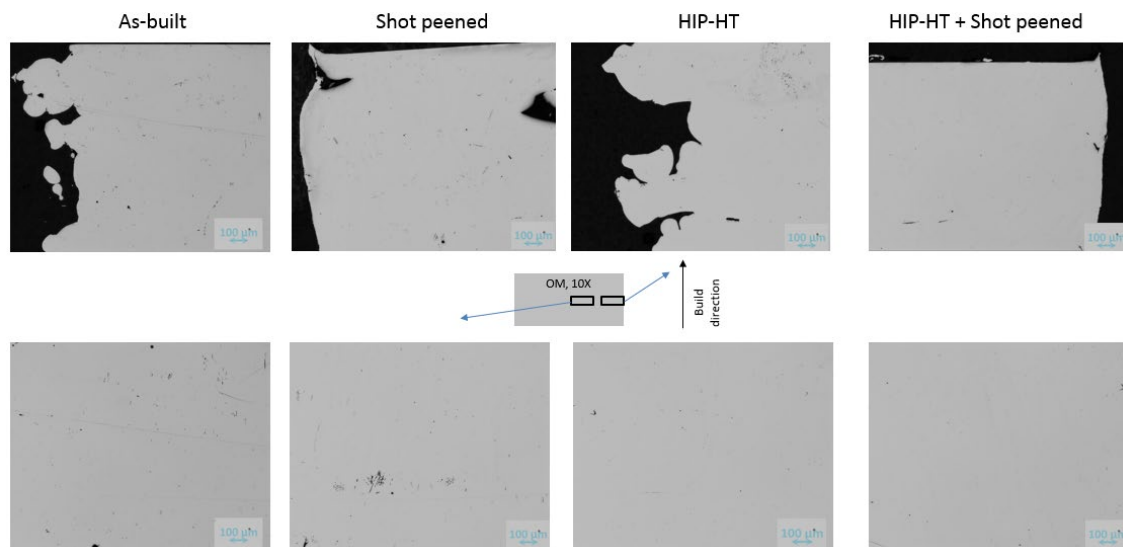


Figure 5.3: OM micrographs showing porosity of different samples.

5.4. Scanning electron microscope (SEM)

Principle of operation of SEM with respect to electron movement is similar to EB-PBF, which has been explained in *section 2.3*. The only difference is that SEM uses a deflection lens for directing the beam onto the sample and a scanning coil to view the optical image formed by the electrons. Different regions on the sample are viewed by moving the sample itself. The electrons upon hitting the surface of the sample's cross-section, most of them undergo scattering and a few undergo transmission. Electron transmission does not fall within the scope of this study. There are different detectors (*see Figure 5.4*) available to capture the electrons for screening, that can be employed depending upon the least position required. Of all these detectors, the ones used for this study are backscattered electrons (BSE) and secondary electrons (SE) detectors. *Hitachi* and *Zeiss* SEM's were used to study the pre and post-exposed samples, respectively, and the following parameters were selected (*see table 5.1*). BSE and SE detectors were used to study the microstructure and topography of the samples, respectively.

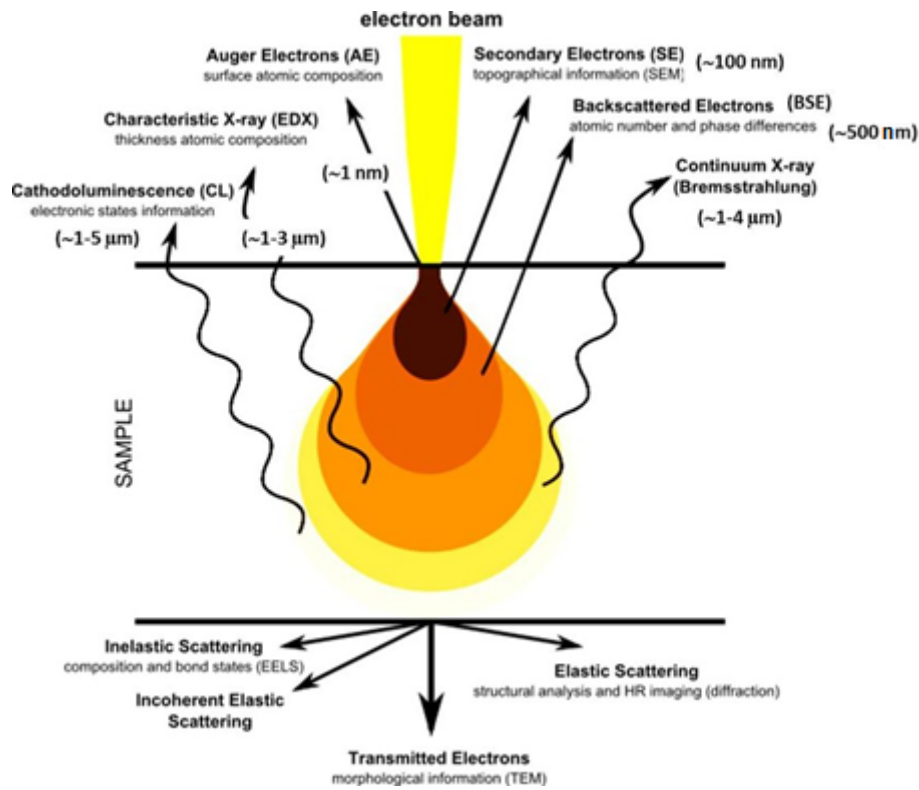


Figure 5.4: Schematic diagram showing different detectors of SEM.

Image courtesy: Ankur Chauhan[29]

The electrons detected by BSE are those electrons that do not lose any of their energy upon collision. The electrons emitted from the beam hit the material atoms with a high kinetic energy that is converted into potential energy during the moment of impact, which is again converted into kinetic energy due to repulsion. Due to this phenomenon, the kinetic energy of the electrons after the collision is restored. Also, there is a shift in its trajectory, which is finally captured by the detector. Due to the widespread of the area of interest due to change in the pathway of bombarded electrons, these electrons carry information of the sample approximately about 500 nm above the surface. More the number of protons more is the electron accumulation on the material upon collision from the beam. Since the BSE detector captures the electrons from the material, the

luminescence of the image data increases with an increase in atomic number. Henceforth, heavier the element brighter the image appears. Due to this dependency, phases, composition, and high element concentration zones can all be identified. This aspect has proven to be useful for identifying Nb-rich zones and grain size measurement, because of the difference in brightness and appearance of grain boundaries, respectively.

Table 5.1: Selected parameters for SEM and EDS

Parameters	SEM	EDS
Signal	NTS BSD, SE (topo)	NTS BSD
Electron high tension	20 KV	15 KV
Filament target	2.697 A, 2.593 A (topo)	2.703 A
Beam current	100 μ A	80 μ A
Scan speed	7	7
Noise reduction	Line average, N = 7	Line average, N = 7
Working distance	9 mm, 10 mm (topo)	7.5 mm
Probe size and spot size	100 – 900 pA and 390 - 514	5.3 nA and 614
Dead time and number of frames	-	23% and 10

The electrons detected by SE are those electrons (*as shown in Figure 5.5*) that are emitted from the material due to the excitation caused by the accelerated electrons from the beam source. Since the electrons that are captured by the detector are from the material itself, they can provide detailed information about the features and curvatures on the surface, which comes from approximately about 100 nanometers above the surface. This detector is used to study the topology of both pre and post exposed samples and has far better accuracy than the BSE.

5.4.1. Energy dispersive X-ray spectroscopy (EDS) for elemental analysis

Whenever there is a release of secondary electrons from the material (*see Figure 5.5*), electron within the material atom comes down from a higher to a lower energy level to remove the accelerated electrons out from the lattice. When the electron residing in the material changes its orbital to a lower configuration, it emits some form of energy called the X-rays. EDS detector converts these X-rays into electrical voltage, which is then viewed as an electron map. Since the valency of every element is different, the voltage produced also varies from element to element. Distinctive electron image generated from different elements of a sample can be mapped together or kept separately either at a point or along a line or a surface of interest. Point maps also provide the concentration in terms of weight percentage for required elements on the desired point. 18 points were selected (*see Figure 6.35*) in total, of which 9 on the oxide layer and 9 below, to consider

the direction of oxidation growth. These mapping techniques have been used to study the elemental distribution of exposed samples.

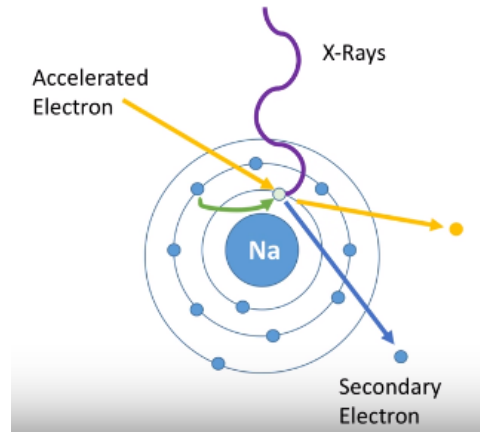


Figure 5.5: Ejection of SE and X-ray emission upon excitation.

Image courtesy: Emily Krull, Oxford Instruments, UK

Closer the electron is to the nucleus of the material atom, more the stability of the shell, greater is the binding energy required to remove that electron. Hence, much less energy is enough to knock out the electron from a higher energy band, with that element in the material releasing a very high amount of energy in the form of X-ray emissions. At this point, X-ray energy can be higher than the ionization energy, and hence, the generated voltage in the detector is a distinctive maximum. The maximum electron count has been marked with an 'X' (see Figure 5.6), by Ni atom, which is the major constituent of Alloy 718. The ratio of measured voltage to the applied voltage apart from the electronic configurations of the elements also depends upon mass absorption coefficient, specimen density, and specimen thickness. Traces of Au is also seen on the histogram due to gold sputtering for a thin layer about 5 to 10 nm above the surface of the sample to avoid image shifting.

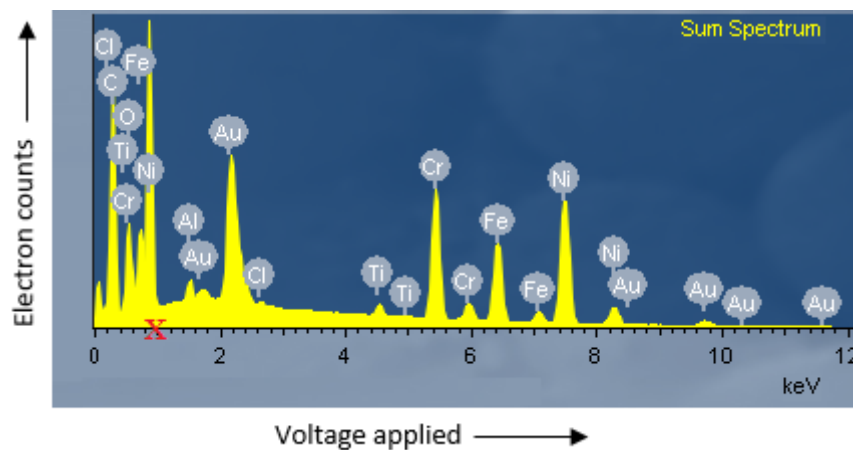


Figure 5.6: Curve showing the electron counts for different elements across different voltages.

5.4.2. X-ray diffractometry (XRD), Residual stress measurement

An XRD consists of an X-ray and a detector that revolve around the sample, having a fixed angle between them, with the sample being stationary. One series of slits are placed in between the

filament and the material, and the other slit series of slits are placed between the material and the detector. These slits are named as (1) and (2) as shown in *Figure 5.7*, which can also be called primary and secondary optics. Primary optics are used to ensure that the beam falls on the plane, narrow the peak, control the beam width, and filter unwanted radiations. Secondary optics are used to reduce scattering of X-rays, limit beam height by reducing axial diversion, remove diffused scattered X-rays from elements of the previous experiment and filter white radiations and other higher β energy level emissions. The distance between the two consecutive planes' of the sample can be ascertained from Bragg's law by knowing the wavelength of an incident electron beam and, either angle ' ω ' between the material and X-ray tube (XRT) or angle ' θ ' between the material and SE beam. Either of the two angles by knowing one can be deduced by the relationship ' $\omega = 2\theta$ '. The strain ' ϵ ' in the material can be computed by moving the XRT and detector around the sample and finding the change in ' d ', as $\epsilon = \Delta d/d$. Residual stresses are measured at different locations in the sample from their corresponding strain values by knowing the modulus of elasticity of the material. Residual stress measurements were carried out by *Linköping University, Sweden*.

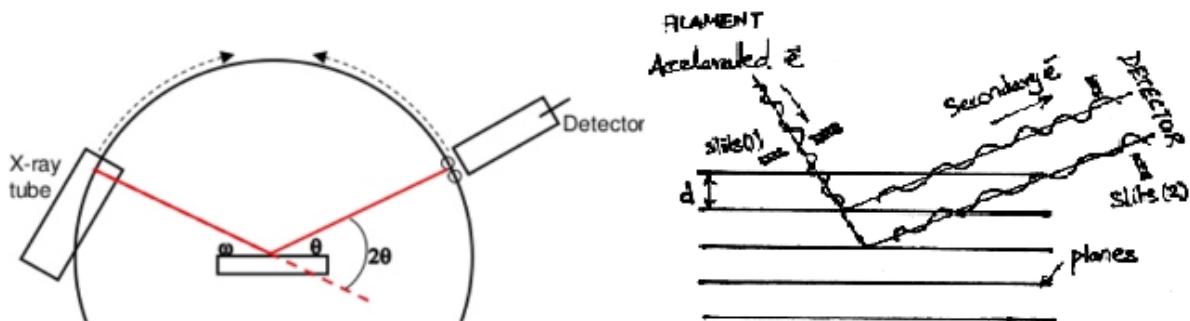


Figure 5.7: Experimental set-up and principle of XRD.

Image courtesy: Emily Krull, University of Toledo, USA

5.4.3. Electron backscatter diffraction (EBSD), Orientation and texture analysis

The positioning of the XRT and the detector is similar to that used in XRD measurements. However, one difference in EBSD is the sample is tilted at an angle (see *Figure 5.8*) of about 7 degrees with respect to horizontal. EBSD is also governed by Bragg's law, just like XRD. In this diffraction technique, only about ~ 20 nm of depth is examined for obtaining the following crystallographic information, namely a) grain orientation, b) grain size and c) grain shape from the sample. When the sample is oriented at a glancing angle, the electrons upon striking the sample, it partially loses its kinetic energy before undergoing diffraction. These diffracted electrons upon reaching the phosphorous compound emit visible light by absorbing the electrons and create a scintillating effect. Depending upon the lattice plane orientations the diffraction pattern changes that are captured by the scintillator, which is the detector here. Change in the diffraction pattern is recorded by comparing all the points of one diffraction pattern with others. Each of these points corresponds to an electron captured by the detector, whose data is processed by the position or angle between the perpendicular line drawn from the point to the sample and the sample. These individual data points for different patterns are plotted, and their corresponding relative positions are compared using computer algorithm after inputting the material properties. Each pattern corresponds to an orientation that has specific Miller indices, and each electron corresponds to a

pixel of the image. All these patterns are mapped together to form an image depicting various crystallographic orientation present within the region of interest. Smaller, the distance between consecutive patterns or step size more is the acquisition of information. Some regions in the grain boundaries appear to be completely white since there are more than one crystal or cell, which cannot be processed by the computer. Hence, the accuracy of crystallographic data depends on the resolution and step size. EBSD measurements of the samples for grain orientation and grain texture analysis was carried out by *Chalmer's University, Sweden*, to quantize its crystallography (see Figure 5.8). Grain texture is the distribution of different grains by forming grain boundaries between them due to the difference in crystallography. Phase quantization can be made by knowing the crystallography of the sample by comparing it with the family of *Miller Indices* of the phase.

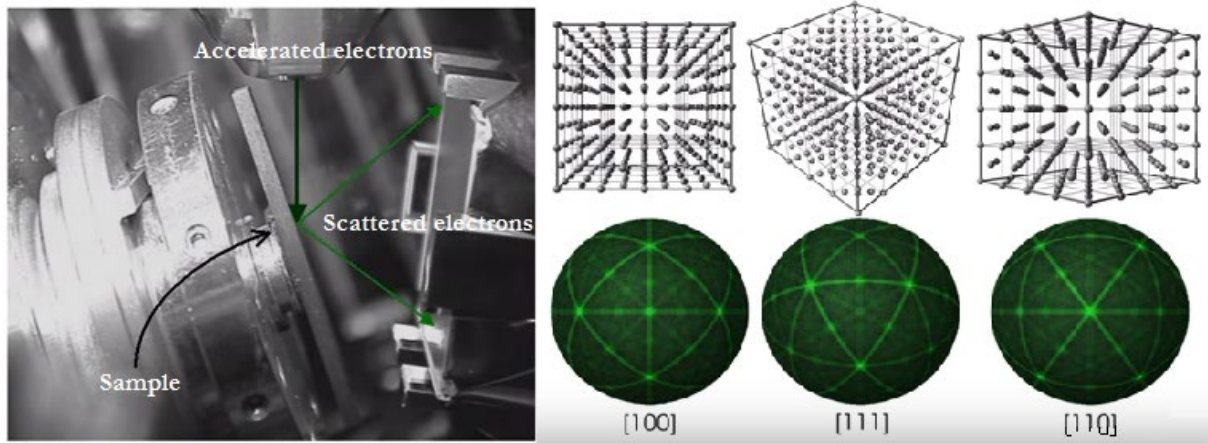


Figure 5.8: Image (left) showing the experimental set-up and image (right) showing different crystallographic orientations that can be measured.

Image courtesy: NPL, UK

5.4.4. Line roughness measurement

An attempt was made to measure the line roughness for the entire sample length of ~ 10 mm by selecting 149 equidistant points on the mean line and finding their peak values in *power point*. These points were selected along the surface of the sample on an SEM image with 50X magnification. Line roughness parameters include arithmetic mean deviation ' R_a ', root mean square ' R_q ', maximum profile height or maximum peak to valley distance ' R_t ', and skewness ' R_{sk} '. $R_a = (1/n) \sum |y_i|$ to find the overall surface roughness, $R_q = [(1/n) \sum y_i^2]^{(1/2)}$ to have more accuracy when the deviations are minimal, $R_t = (y_i)_{\max} - (y_i)_{\min}$ to know the overall height of roughness profile and $R_{sk} = (1/n \cdot R_q^3) \sum y_i^3$ to know the symmetricity, ' y_i ' peak height at a position ' i ' and ' n ' is the total number of points. The same parameters can be used to measure the surface roughness by finding the cumulative average for a series of line roughness values within the specified region.

5.4.5. Effect of post-processing

SEM images in 50X magnification were obtained for all the samples, indicating the contour-1,2 and hatch regions to study the effect of post-processing on pre-exposed samples. However, the

effect in the hatch region is not considered in this study. Effect of HIP-HT and shot peening can be seen in *Figure 5.9*.

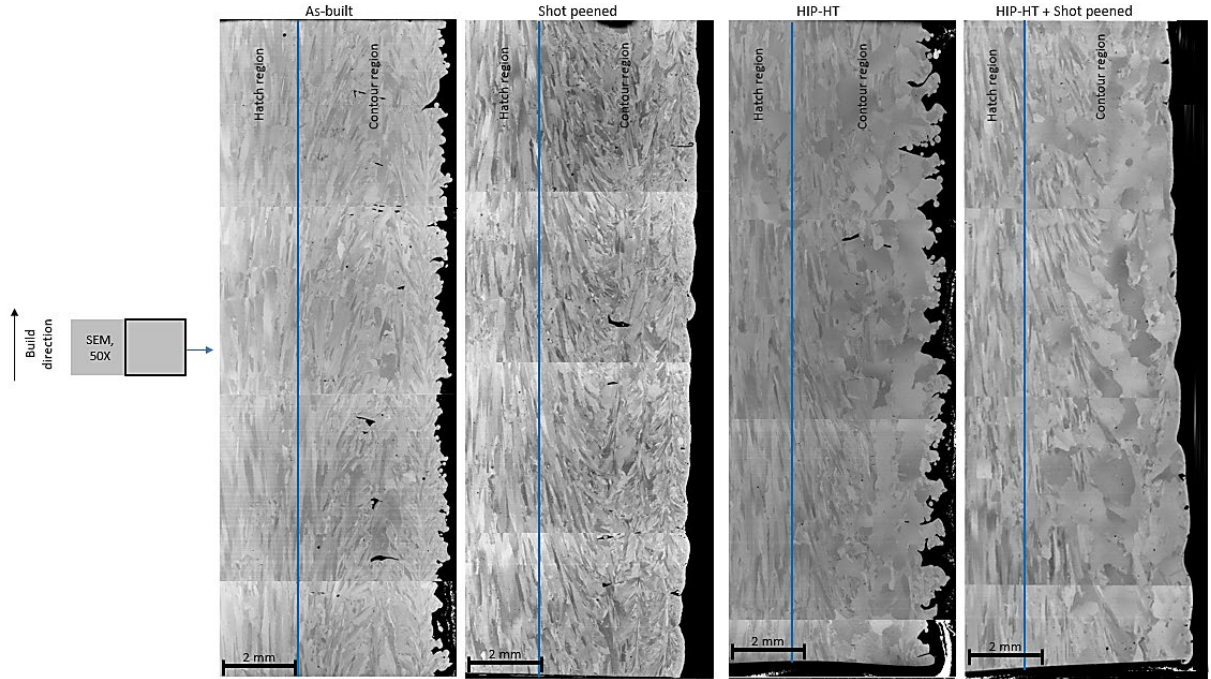


Figure 5.9: SEM images (BSE mode) showing different zones (contours and hatch) for each sample.

5.4.6. Grain size measurement

Grain size was measured (*see Figure 5.13*) for all the samples according to the *ASTM E112* standard using the line intercept method. However, with one difference is that measurements were done in parallel lines along the x-axis, to see the effect of the transition of grains from equiaxed to columnar due to shot peening (*see figure 5.11*). The SEM images of different magnifications ($M \neq 100X$) were taken for the samples, along the contour region (*see Figures 5.10, 5.11 and 5.12*). The ASTM number 'G' (applying \bar{l} in millimeters) and the number of grains per square inch of area for M magnification ' n_M ' was calculated for each sample. Grains per square micrometer was calculated (from its equivalent square inch) for the same magnification to have better accuracy. Smaller the size of grains, more can it be accommodated for the same area and magnification. Hence, n_M value

decreases with increasing grain size. Extraction of ASTM number and n_M is given in *table 5.2* for reference.

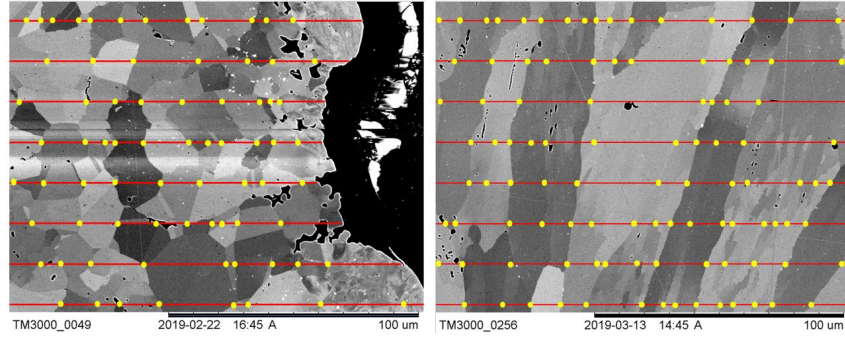


Figure 5.10: Image showing the grain intersections along a series of horizontal lines.

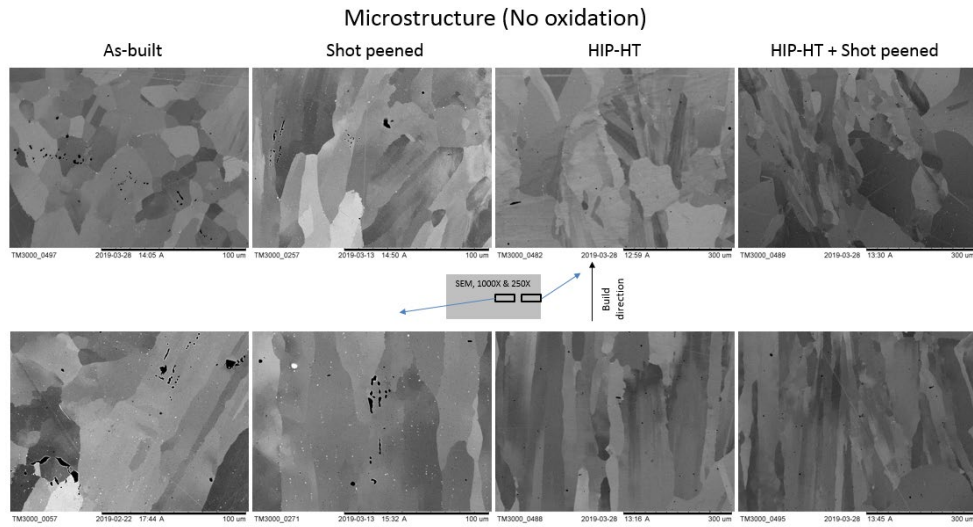


Figure 5.11: SEM (BSE mode) images showing the microstructure of pre-exposed samples.

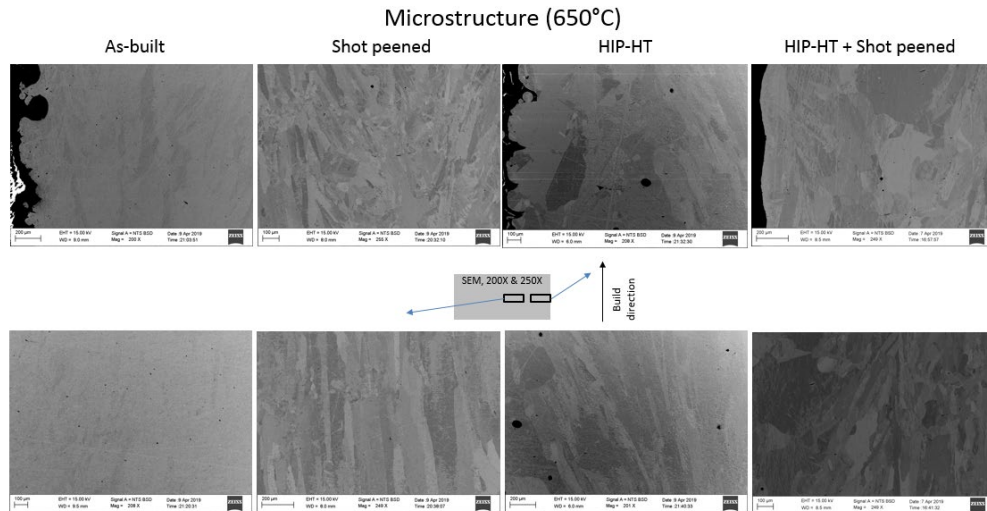


Figure 5.12: SEM (BSE mode) images showing the microstructure of exposed samples at 650°C after 168 h.

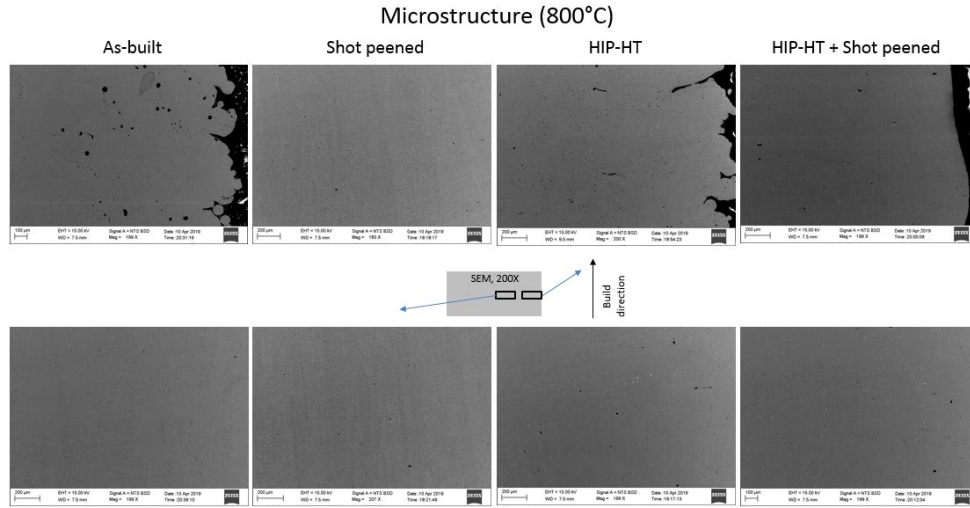


Figure 5.13: SEM (BSE mode) images showing the microstructure of exposed samples at 800 °C for 168 h.

The formulas used for determining the grain size are as follows (that are in direct reference to *ASTM E112-113* standard):

- Magnification, $M = \frac{\text{length of scale bar measured in mm and converted to } \mu\text{m}}{\text{number next to scale bar in } \mu\text{m}}$
- $\bar{l} = \frac{(\text{total length of lines in mm})}{(\text{number of grain boundary intersections}) \cdot (\text{magnification})}$
- $G = -6.6457 * \log(\bar{l}) - 3.298$
- $n_M = (2^G - 1) \cdot (M/100)^2$

Table 5.2: Grain size calculation

Sample	Magnification (M)	Total length of line at 'M' (in mm)	No. of grain boundary intersections	\bar{l} (in mm)	G	n_M per inch ²	n_M per μm^2
As-built	121X	1530	335	0.0378	6.1570	52.36	8.11e-08
Shot peened	121X	1539	464	0.0276	7.0742	99.55	1.54e-07
HIP-HT	300X	1600	55	0.1000	3.3956	50.70	7.86e-08
HIP-HT + shot	300X	1600	72	0.0905	3.6506	83.35	1.29e-07

5.4.7. Niobium-rich phase content

The SEM images (BSE mode) with 3000X magnification was selected for both pre and post exposed samples (see Figures 5.14, 5.15 and 5.16) along the contour region. The Nb-rich phase content was identified by observing the bright sections (see section 5.4) in the SEM-BSE images, as it is a heavy element in Alloy 718. The grain morphology was not considered, and hence only the quantization of Nb by area was performed, but not the quantization of the same for each phase. It is known that Nb contributes to the strength of Alloy 718 by contributing in different phases (see section 3.2).

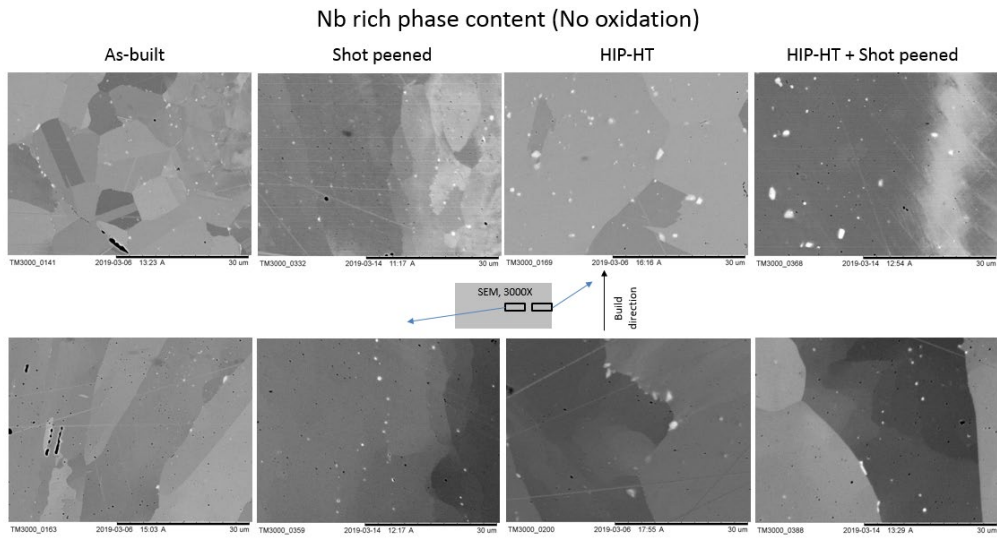


Figure 5.14: SEM images (BSE mode) showing the Nb-rich zones of the pre-exposed samples.

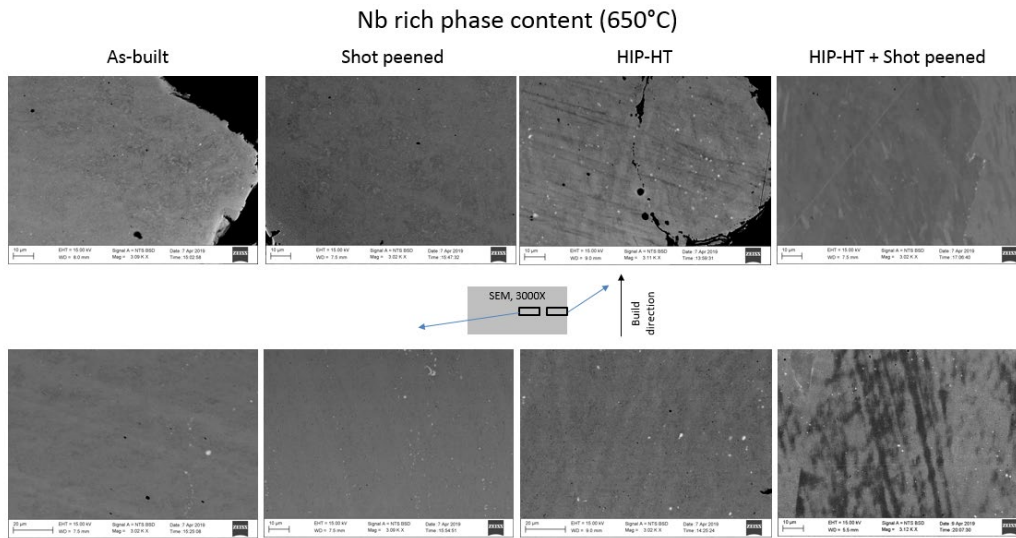


Figure 5.15: SEM images (BSE mode) showing the Nb-rich zones of the exposed samples at 650 °C for 168 h.

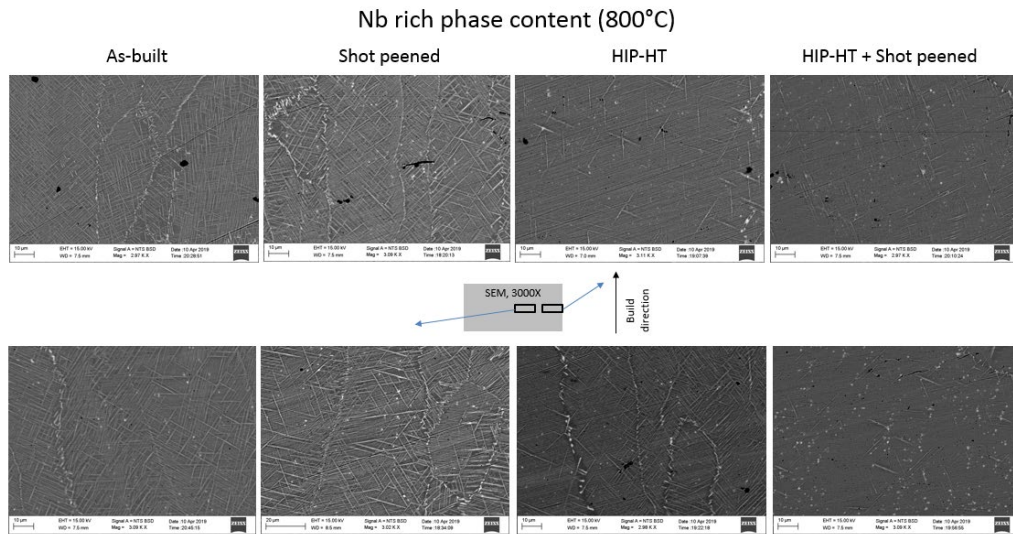


Figure 5.16: SEM images (BSE mode) showing the Nb-rich zones of the exposed samples at 800 °C for 168 h.

5.5. ImageJ

ImageJ is an open software for measuring the particle size by area. It carefully eliminates the background, taking into consideration only the particles by providing a threshold value in *Figure 5.17*. This locks the intensity peak of the image and makes all other intensities fall below it, which is the same as the cut-off frequency provided for vibration data. By providing a threshold input, the required particles are selected, whose area is measured also providing their min., max., and mean values. Porosity for the exposed samples and Nb-rich zones for all the samples were measured using *ImageJ*. Porosity has a dark spot as it is the lightest region since there are no materials in the void space whereas, Nb has a bright spot as said before (*section 5.4.7*). Because of this bright and dark spots, opposite threshold must be provided for both measurements, respective to each other. Only color option available for highlighting the pixels (i.e., region) of interest is red. Other inclusions were eliminated by using the paint tool to cover them in either black or white that favors spot intensity. Another way of elimination was by using a polyline to cover the area without any inclusions.

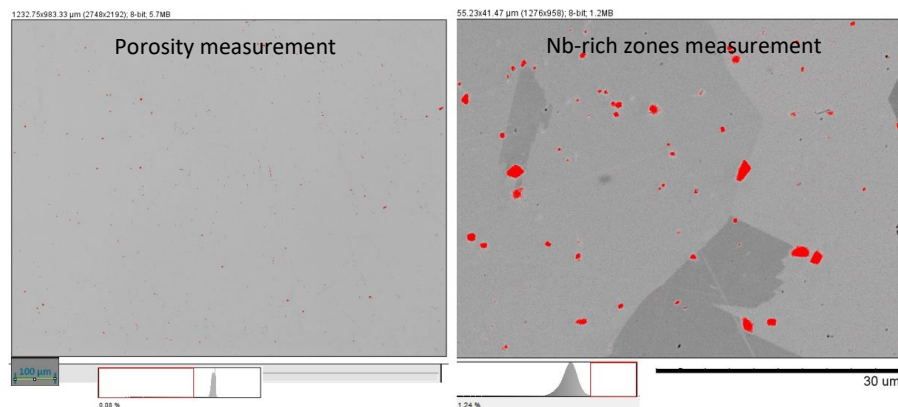


Figure 5.17: Highlighting porosity and Nb-rich zones using ImageJ.

5.6. White light interferometry (WLI) for topographical analysis

The white light emitted by an LED that is passed through the condenser lens, changing the divergent beams from the light source to a parallel set of beams. These beams upon going through the beam splitter are divided into two halves. One-half is made to fall on the focus lens and the other on the objective lens. The beams start converging after passing through the objective lens, which before becoming fully converged, the narrow beam passes through the secondary beam splitter that is placed closer to the sample. This narrow beam completely converges at both the sample and reference mirror due to splitting. Upon the beam reflected from the sample interacting with the one reflected from the mirror, the sample beam undergoes a phase shift. This beam, when fed back to the focus lens is converged along with the continuum of white light from the source, interferes with each other forming an interference pattern, which is recorded by the charge-coupled camera. This camera converts this visible spectrum from the white light, into electrical signals for digital imaging from which required surface information can be extracted. Experimental set-up for (WLI) has been depicted in *Figure 5.18*.

All the inputs and outputs are provided using software and a computer. The position of the mirror is fixed while the camera can move along the z-axis, and the sample can move that is mounted on a bed can move both in x and y-axis. Focus points can be adjusted by moving the camera, and the required region of interest can be acquired by the movement of the sample. The camera is attached to the stepper motor, whereas the objective is attached to piezoelectric crystal for highly precise motion. WLI or 3D profilometry was done using [Filemetrics ProfilM 3D](#) equipment to study the surface roughness, surface finish, surface profile, and area of the particles belonging to the surface texture. Surface parameters measured include S_a , S_q , S_t , and S_{sk} that are similar to line roughness (see section 5.4.4). Note that surface texture mentioned in sections 2.4.4 and 5.6 is different from the grain texture referred in section 5.4.3. Different parameters and filters were selected (see table 5.2) for each sample to have the best possible output.

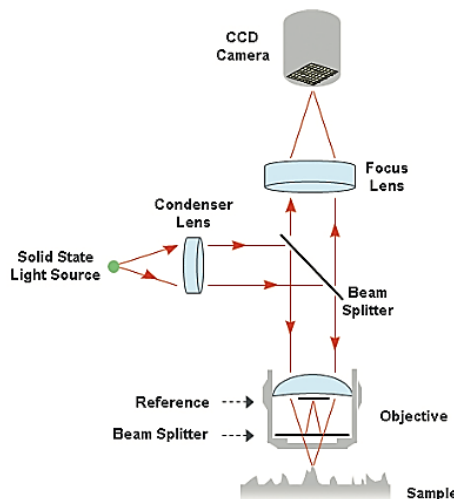


Figure 5.18: Schematic showing the working principle of WLI.

Image Courtesy: [Nanoscience Instruments, USA](#)

Table 5.3: Selected parameters and filter for 3D profilometry measurements

Parameters	As-built	Shot peened	HIP-HT	HIP-HT + shot
Magnification	10X	10X	10X	10X
Zoom	1X	1X	1X	1X
Valid pixels	15.17%	50.75%	16.82%	37.62%
Area covered (μm^2)	(3000 x 3500)	(3000 x 3500)	(3000 x 3500)	(3000 x 3500)
Envelope threshold	center, 1%	center, 0.95%	center, 1%	center, 0.95%
Backscan (μm)	355	194	450	298
Scan length (μm)	720	390	1000	600

Filters	As-built	Shot peened	HIP-HT	HIP-HT + shot
Flatten	plane flattened	plane flattened	plane flattened	plane flattened
Spatial filter	median, 7x7	median, 13x13	median, 7x7	median, 13x13
Fill in invalids	interpolation	interpolation	interpolation	interpolation
Remove outliers	max. 85° slope	max. 75° slope	max. 85° slope	max. 75° slope

Valid pixels depend on the surface finish of the material, the more lustrous it is, the more is the reflectivity of the sample, and hence more pixels due to improved interference. Backscan and scan length is set after knowing the deepest valley and the highest peak, by moving the scan head. Upon focusing the camera on the sample, a sharp image of the peaks is produced. Table height along both X and Y directions needs to be adjusted such a way that no red spots are seen on the image. Now the camera is focusing the middle of the average of peaks, which when moved upward, produces a fading image than becoming blurred with just one or a few sharp points and the same when moved downward. This blurred image shows the position of highest and lowest points of the highest peak within the region of interest. After locking the highest position, the head is lowered till the minimum point and the distance traversed between them is set as the backscan, and the range covered by moving the head further to form a completely blurred image on both ends is set to be the scan length. This is done to ensure that there will be no loss of surface information as no information is recorded during backscan, and according to the scan length, the step height is decided by the software, which is then averaged out to produce the results. An envelope threshold (see Figure 6.11) is used to find the minimal variance, here at the center, for fitting the curvature of the correlogram. Unwanted noise that is picked up while scanning is removed using different filters that are briefly described next. (i) Median spatial filter arranges the data in increasing order within the specified size of the pixel matrix, (ii) invalids corresponds to those regions where data extraction was not possible, which are filled by interpolating the peak values from the neighboring pixels, (iii) distinctively high peak(s) are removed by setting the maximum allowable slope with its base still

present that can be smoothened by '(i)', (iv) flatten filter is self-explanatory. Surface roughness parameters after the application of filters were considered.

5.7. Hardness measurement by Vickers microhardness (HV)

Hardness is the measure of the strength of a material by knowing its ability to withstand a specified magnitude of force imposed on the workpiece with indenter of required geometry and size for a specified duration. Discussions and theories from here in this section except the parameter selection have been directly referred from *ASTM International, USA* [30]. Force is imposed by plunging action of the diamond indenter with a geometry specified by the dimensions ' d_1 ' and ' d_2 ' forming the two diagonals as shown in *Figure 5.19*. There are two types of hardness tests, namely, micro-indentation and macro-indentation hardness tests. Load limits for the former is between 1 to 1000 gf with $d_1 = d_2 (=d)$ and that for latter is > 1 kgf with $d_1 \neq d_2$.

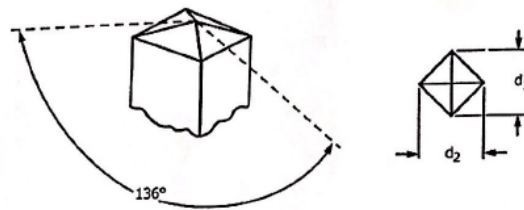


Figure 5.19: A diagram showing the indenter for measuring HV.

Image courtesy: ASTM International, USA

Vicker's micro-indentation hardness test with a force ' P ' of 4.903 N (i.e., ~ 500 gf) for a duration of 15 seconds was carried out for each indentation. Experiments to determine HV values for all samples were done according to *ASTM E384* standards. A total of 30 indentations with five spots along the length of the sample with an equal spacing of 200 μm starting from the surface and six spots along the width of the sample with an equal spacing of 1300 μm to 1400 μm , was done for each sample to obtain the hardness values. Hardness values are calculated from the equation, $HV = 1854.4 \cdot (P/d^2)$ that has been obtained from the known face angle of indenter ' α ' = 136° and trigonometric relations from the geometry. ' d ' (in mm) is calculated after indentation by the software. Unit (gf/mm²) can be termed as 'HV'.

5.8. Oxidation exposures

All the post-processed samples, along with as-built, were placed inside a furnace with atmospheric oxygen after measuring their surface area and weights. The samples were weighed again after removing them from the furnace after a stipulated duration to determine the weight gain. Samples before and after conducting exposure tests are shown in *Figure 5.20*. For obtaining the curved surface area (CSA), the particle area of surface texture (*refer 2.3.4*) of each sample was determined from WLI for an area of 0.105 cm² which was then extrapolated to the CSA assuming no surface texture. This was done to take into consideration the influence of surface features on weight gain by area. Similar extrapolation was not done for perimeters as it has been machined, having a flat surface unlike the CSA of the sample. EDS analysis was performed using *Zeiss SEM* for point, line, and surface mapping (*refer 5.4.1*) of all the 168-h exposed samples. However, EDS was not performed for 96 and 336-h samples as they were employed only to find the trend in weight gain.

The oxide layer thickness was also measured for the 168-hour exposed samples by using the digital scale in SEM software. A similar digital scale is available in OM software as well.

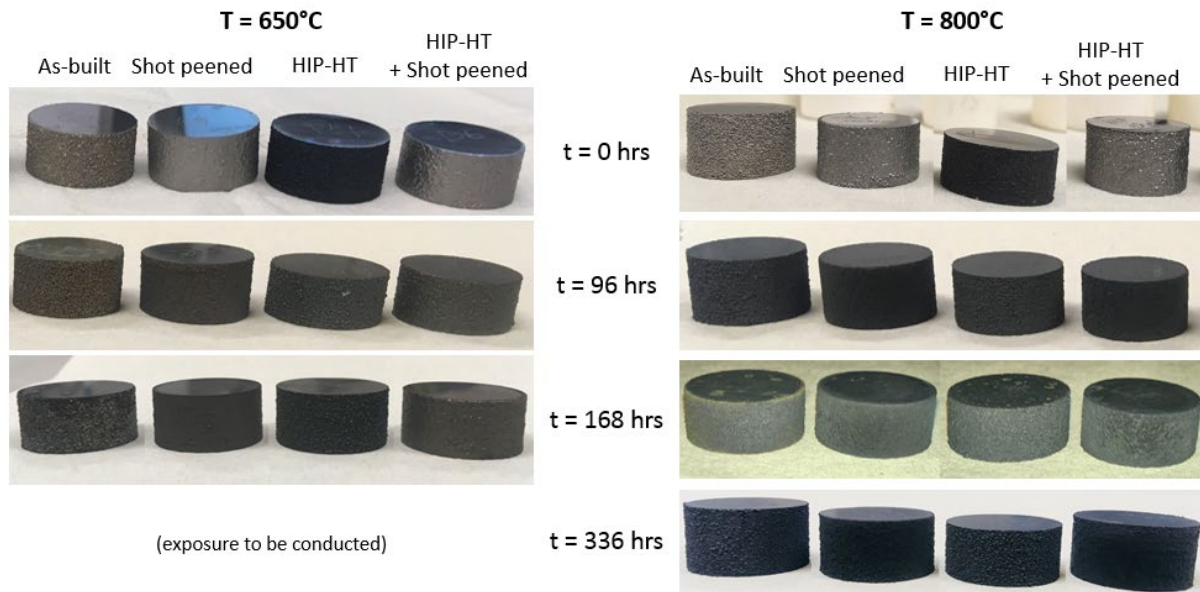


Figure 5.20: Picture of the samples before and after exposure for different temperatures and durations.

6. Results and discussion

6.1. Material characterization

Values for different material properties have been recorded for all the pre-exposed samples in *table 6.1*. Weight gain at different temperatures & durations for all the exposed samples with crucible has been recorded, that is indicated in *Figures 6.19, 6.20 and 6.21* & without crucible for the same is indicated in *Figures 6.22, 6.23 and 6.24* on the bar. Nb-rich phase content values were also recorded for the exposed samples, which has been indicated in *Figure 6.2* above the bar. Values are provided for all other charts as well for better comparison when there is a minimal difference between the data.

Table 6.1: Characterization of the pre-exposed samples

Sample	Grain size (n_M per μm^2)	Nb-rich phase (in % area)	Porosity (in % area)	Hardness (in HV)
As-built	$(8.11 \pm 0.5) \text{ e-}08$	0.26 ± 0.12	0.49 ± 0.29	405 ± 12
Shot peened	$(15.4 \pm 2.1) \text{ e-}08$	0.24 ± 0.14	0.28 ± 0.14	426 ± 27
HIP-HT	$(7.86 \pm 2.9) \text{ e-}08$	0.65 ± 0.53	0.19 ± 0.19	464 ± 12
HIP-HT + Shot	$(12.9 \pm 2.9) \text{ e-}08$	0.49 ± 0.28	0.16 ± 0.08	469 ± 15

6.2. Grain size

It can be seen from *figure 5.9* that as-built and shot peened samples have more columnar grain structures with the corresponding HIP-HT samples having more equiaxed grain structure. Both as-built and shot peened samples have columnar grains oriented in the form of dendrites, with the former having more uniformity and bigger branches compared to the latter. This is because the grain becomes narrow and longer after shot peening. Value of n_M is inversely proportional to the grain size (explained in *section 5.4.6*). Based on the measurement of number of grains per square micrometer for all the samples, grain size appears to increase after HIP-HT and reduce after shot peening (*see Figure 6.1*).

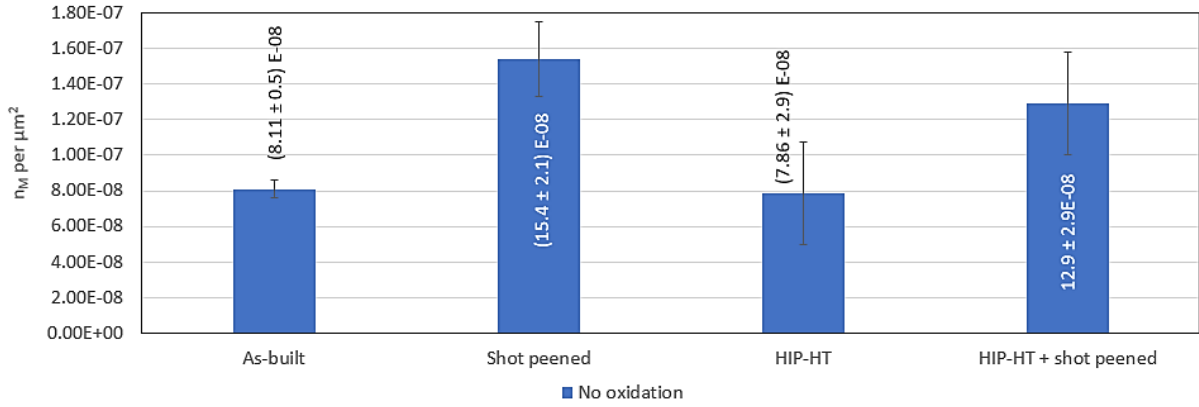


Figure 6.1: Results of the grain size measurement.

6.3. Niobium-rich phase content

HIP-HT showed the highest area of the Nb-rich zones, meaning that there is an equivalent amount of Nb depleted zones in the sample. Effect of Nb in maintaining the strength of the alloy has been discussed in *section 3.2*. It can be observed from *Figure 6.2* that in spite of increasing the strength by HIP-HT and improving surface finish by shot peening, the material without any post-processing has the most homogeneous Nb concentration. However, as told before the strength of the as-built sample cannot be compared with the other post-processed samples as the Nb concentration in each phase is not yet considered. Nb-rich zones decrease by shot peening on HIP-HT sample but not on as-built.

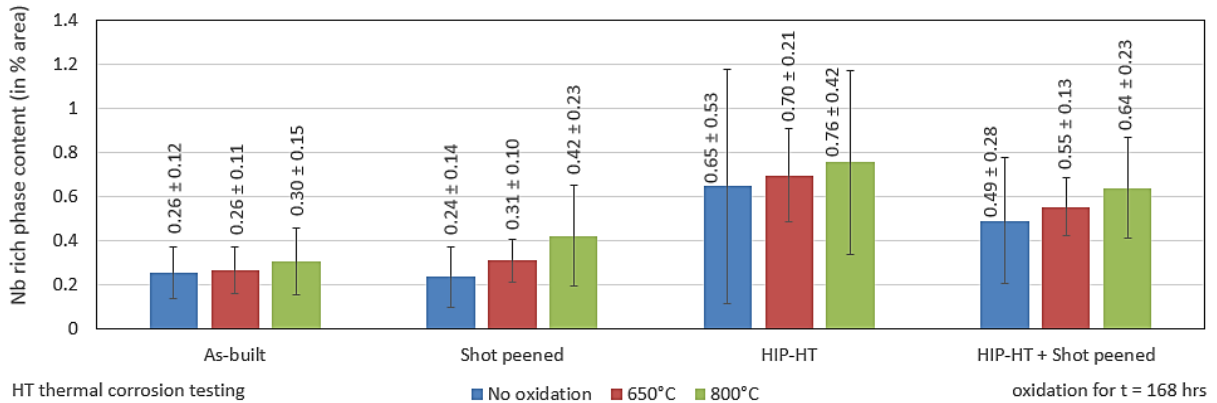


Figure 6.2: Results of the Nb-rich zone measurement.

6.4. Porosity

It is observed that both shot peening and HIP-HT reduces porosity along the contour region, with the least porosity observed in HIP-HT + shot peened sample and highest porosity observed in the as-built sample. However, lack of fusion is still observed with both the post-processing technique having the nearly same effect on it (*see Figures 5.9 and 6.3*).

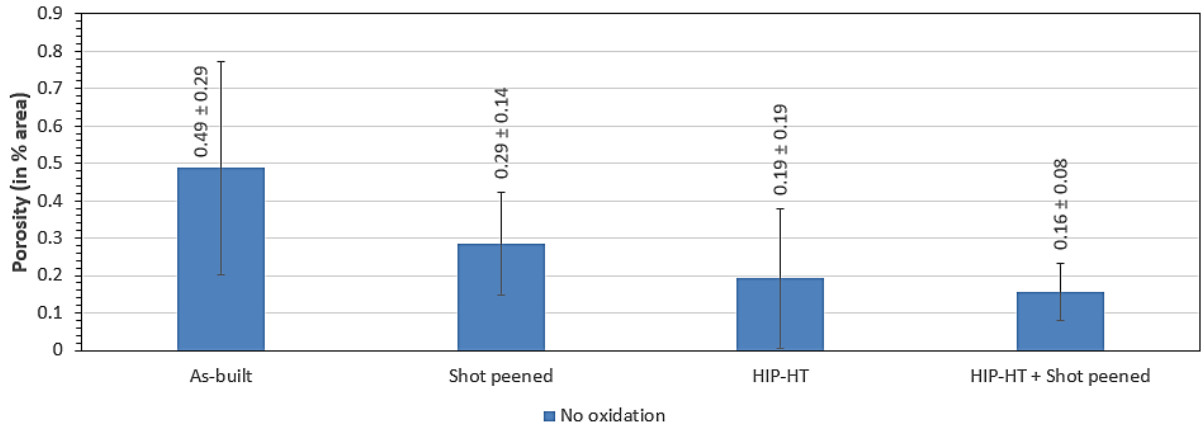


Figure 6.3: Results of porosity measurement.

6.5. Orientation and texture analysis

It is observed from *Figure 6.4* that shot peening changes the grain distribution at the surface, having lesser grain discontinuities. Shot peening also causes grain orientations favoring more intergranular δ sites at the surface. On the other hand, HIP-HT reduces δ pinning.

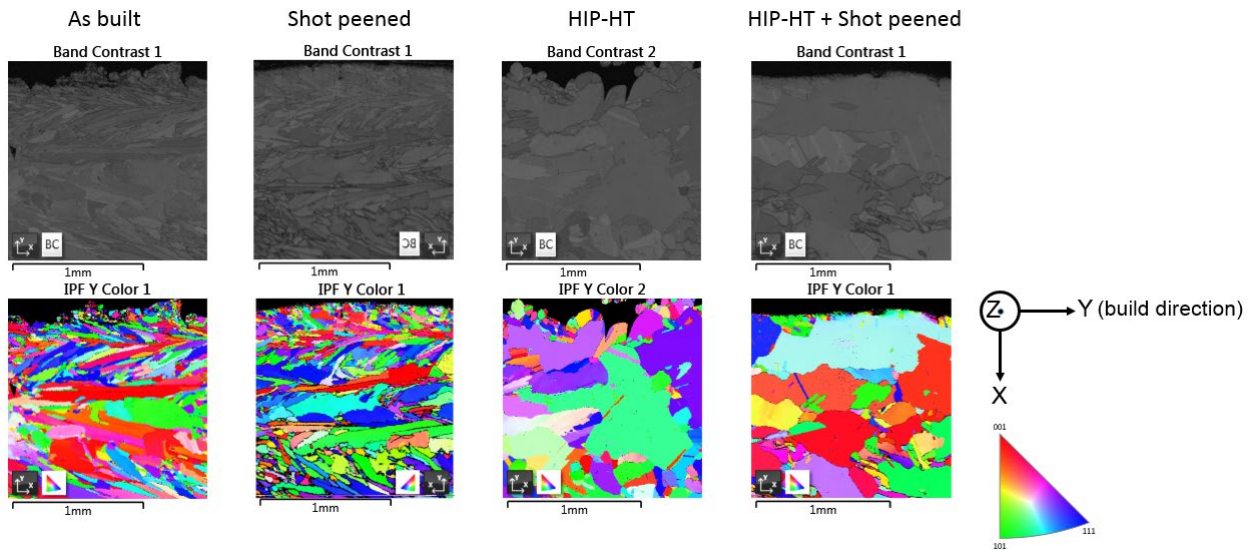


Figure 6.4: EBSD analysis showing grain orientation and texture for all the samples in the contour region.

6.6. Topographical study

As-shot peened samples have the formation of small oval-disk particles (*see Figure 6.6*) on the surface at 650°C with a few needles that grow at 800°C diminishing the disks. Shot peening after HIP-HT has no disk-like particles on the surface with only small needles (*see Figure 6.8*) at 650°C, that grows at 800°C along with the formation of disks of the same shape as observed in the as-shot peened sample. However, only near round-shaped disks (*see Figures 6.5 and 6.7*) are observed

on the surface of both as-built and shot peened samples at 650°C, which grows at 800°C. These needles and disks or globules have no relation with the δ morphology. More clustering of the particles is seen at 800°C for all the samples, which can be due to its growth. These particles can possibly belong to the oxide layer. Scales of oxide layer (see Figure 6.7) is seen by the arrangement of some disks in an array at 800°C for HIP-HT sample. Particles which appear to be like disks belong to NiO or NiOCr_2O_4 , which actually possess a cube structure, and those particles having needle structure are Cr_2O_3 .

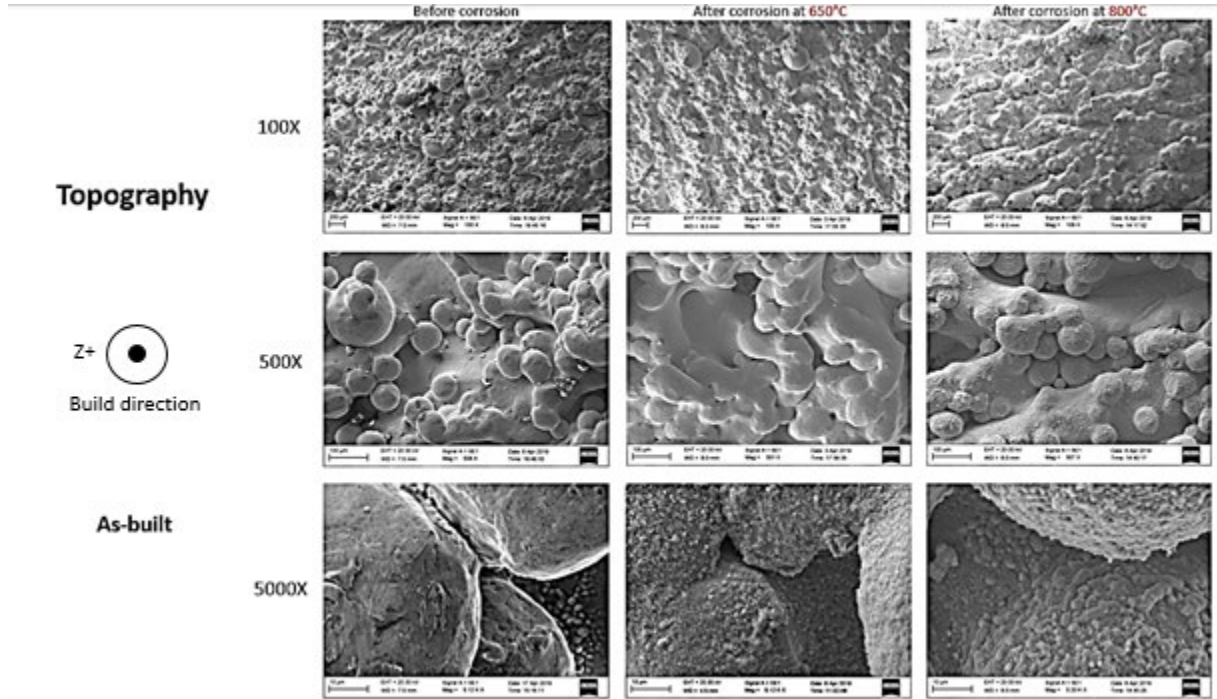


Figure 6.5: Topographical SEM images (SE mode) of the surface of the as-built sample under different magnifications.

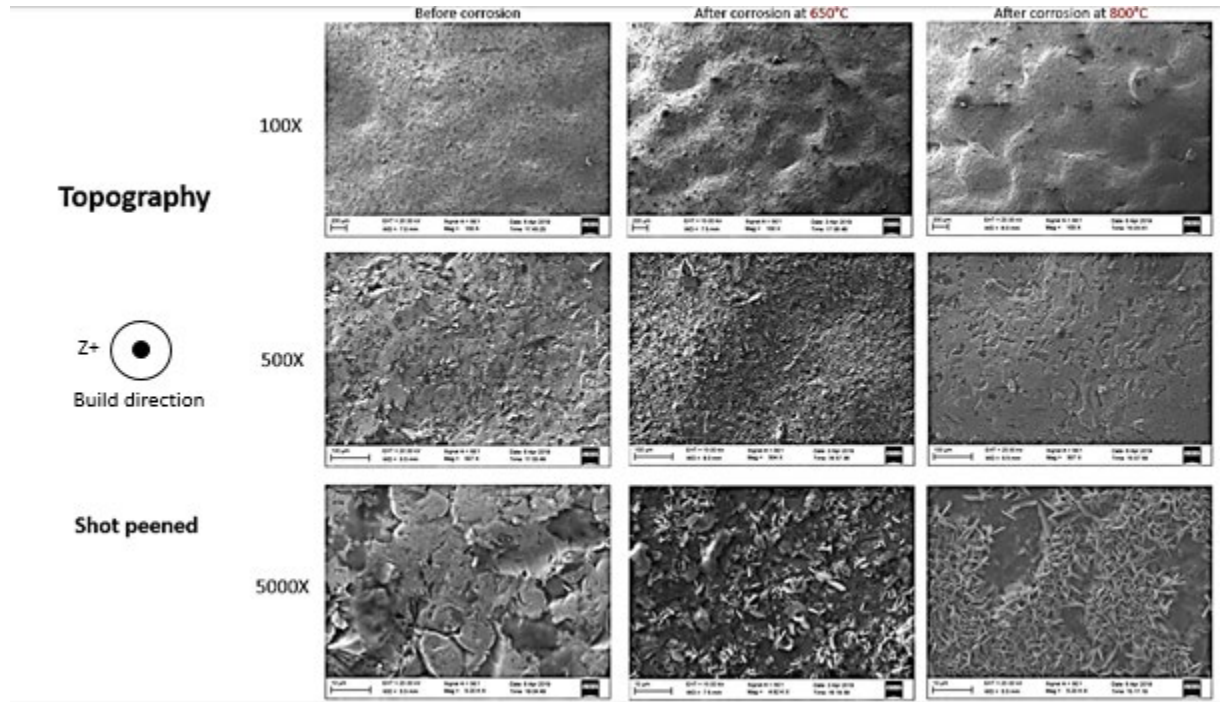


Figure 6.6: Topographical SEM images (SE mode) of the surface of the shot peened sample under different magnifications.

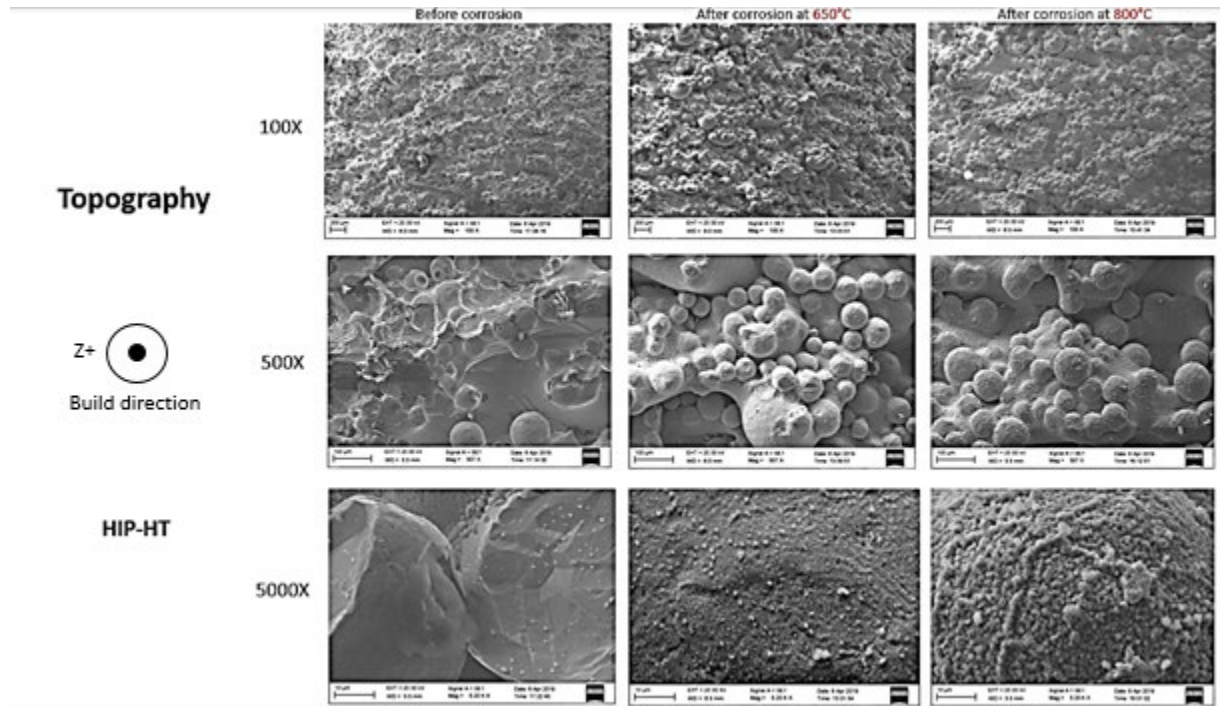


Figure 6.7: Topographical SEM images (SE mode) of the surface of the HIP-HT sample under different magnifications.

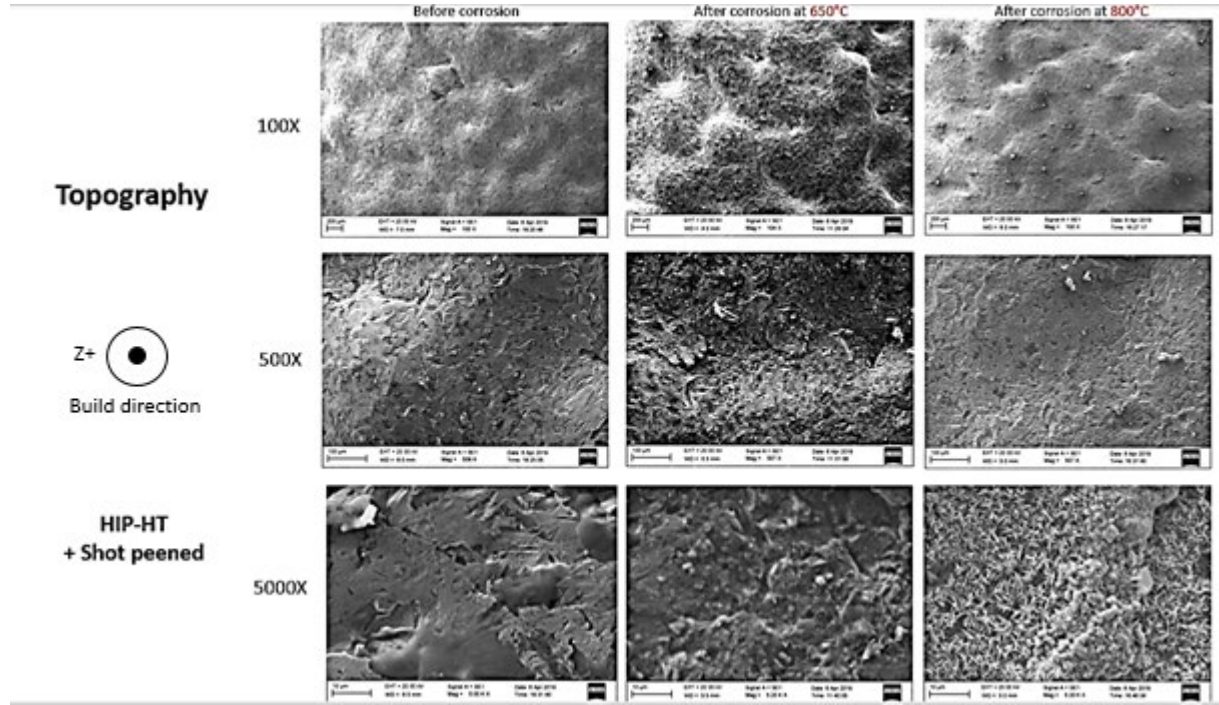


Figure 6.8: Topographical SEM images (SE mode) of the surface of the HIP-HT + shot peened sample under different magnifications.

6.6.1. Line roughness

HIP-HT seem to increase the line roughness while shot peening decreases line roughness (*see Figure 6.10*). Corresponding arithmetic mean (R_a) and RMS (R_q) values had nearly the same difference between the samples (*see Table 6.4*), meaning that line roughness values of all the samples have low standard deviation. *Figure 6.9* shows the spline connecting all the points for line roughness measurement of each sample, thus depicting their corresponding profile curves at any intermediate line segment of surface roughness.

Table 6.2: Line roughness parameters

Sample	R_a (μm)	R_q (μm)	R_t (μm)	R_{sk} (μm)
As-built	49.36	58.32	271	0.0751
Shot peened	20.68	24.09	106	0.9138
HIP-HT	107.48	128.62	593	1.0680
HIP-HT + Shot	27.42	34.21	139	-1.1869

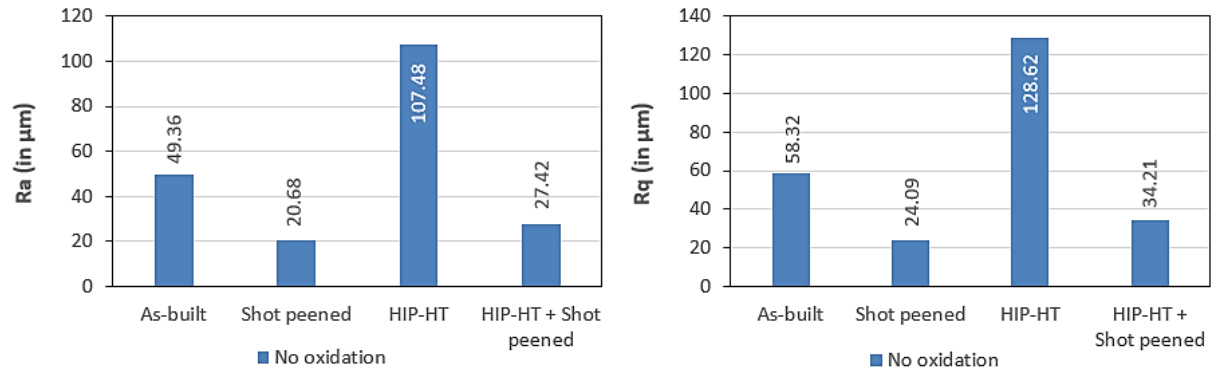


Figure 6.9: Line roughness measurement.

6.6.2. Surface roughness

A trend similar to line roughness was seen in surface roughness, as it is the average of a finite number of line roughness (*table 6.5, Figures 6.12 and 6.13*). However, there was some difference between their magnitudes as the line roughness was measured with an incredibly lower accuracy compared to surface roughness. Both shot peening and HIP-HT tend to increase the symmetry of surface roughness.

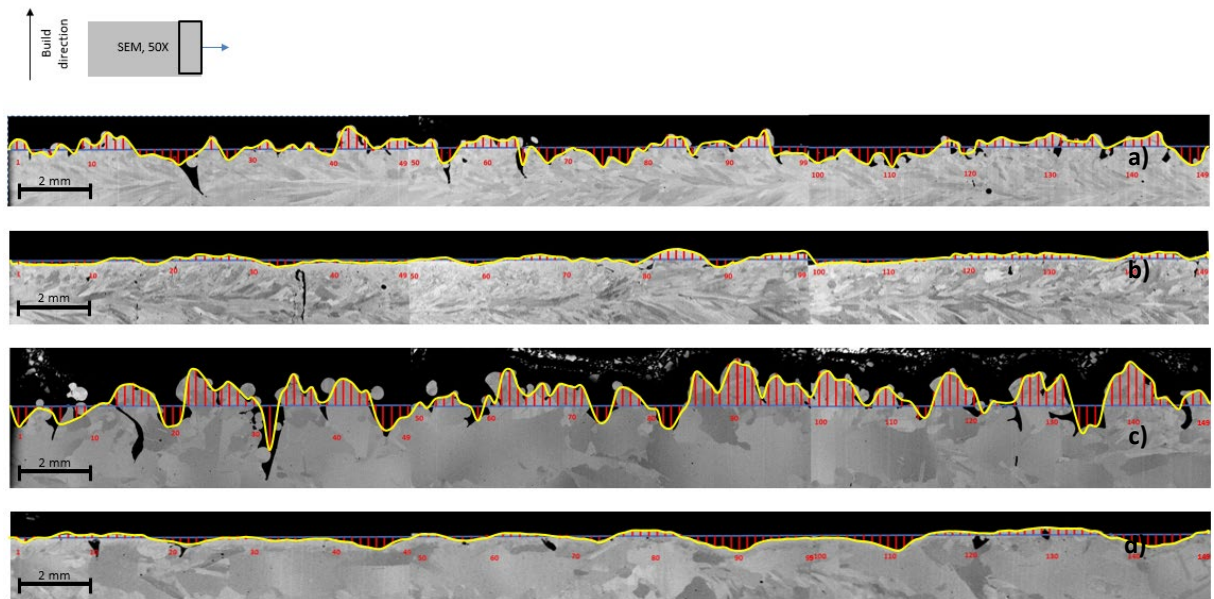


Figure 6.10: Figure showing points selected for the line roughness measurement and profile curves for a) as-built, b) shot peened, c) HIP-HT and d) HIP-HT + shot peened samples.

Table 6.3: Surface roughness parameters

Sample	S_a (μm)	S_q (μm)	S_t (μm)	S_{sk} (μm)
As-built	57.13	70.63	505.1	-0.5568
Shot peened	38.70	46.41	246.3	0.0675
HIP-HT	63.21	77.25	626.7	-0.1461
HIP-HT + Shot	50.68	61.94	342.3	-0.1670

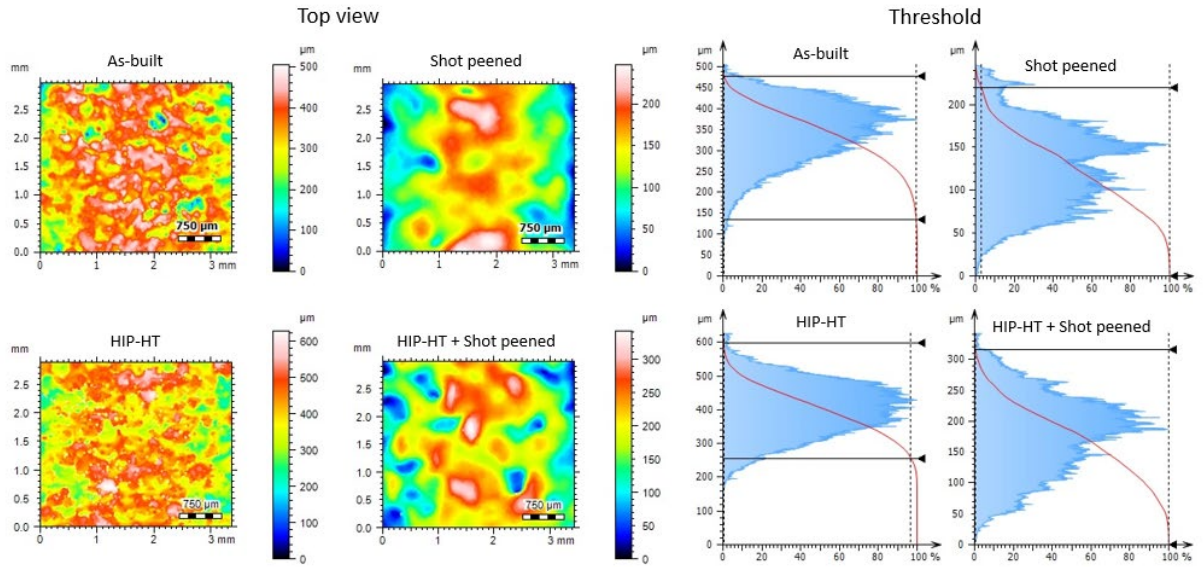


Figure 6.11: Envelope threshold and top view.

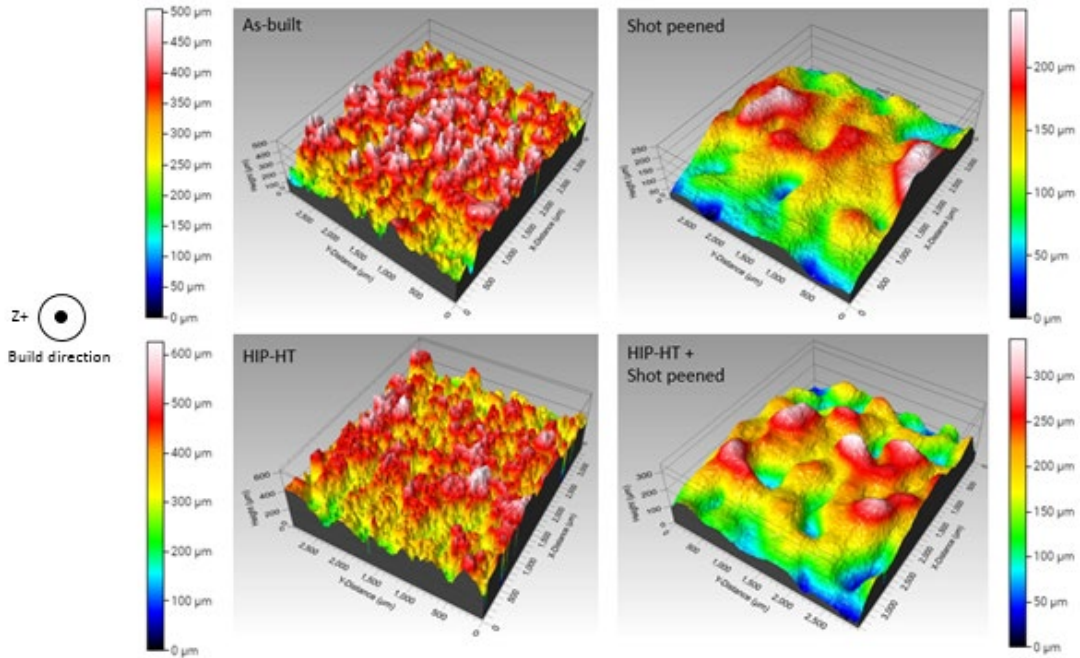


Figure 6.12: Surface roughness mapping.

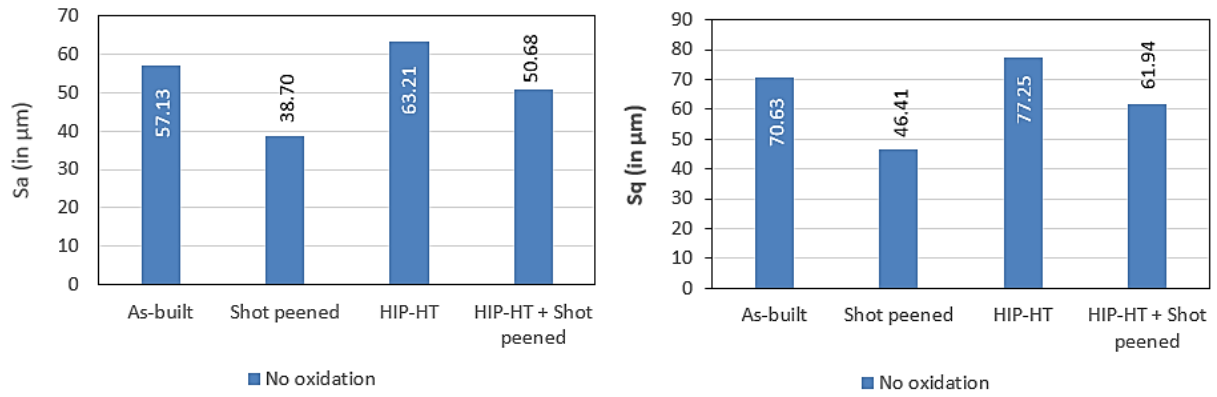


Figure 6.13: Surface roughness measurement.

6.7. Residual stress

It can be observed from *table 6.6* that shot peening has significantly induced a high amount of both axial and hoop compressive residual stresses (*indicated in table 6.6*) for both as-built and HIP-HT samples, with the later having a lower value. The effect of shot peening cannot be compared for both the samples as data is unavailable for HIP-HT sample. *Figure 6.14* shows the direction in which the stresses are applied using X-ray (as discussed in *section 5.4.2*) for which the material is strained in the opposite direction, whose stress values are computed as follows. It can be seen that the as-built sample alone has a possibility of tensile residual stress considering the data scatter with error bars.

Table 6.4: Residual stress values

Sample	Axial stress (MPa)	Hoop stress (MPa)
As-built	-38.8 ± 87.1	-228.8 ± 98.1
Shot peened	-814.8 ± 97.5	-851.1 ± 86.9
HIP-HT	to be measured	to be measured
HIP-HT + Shot	-621.5 ± 72.8	-511.7 ± 82.0

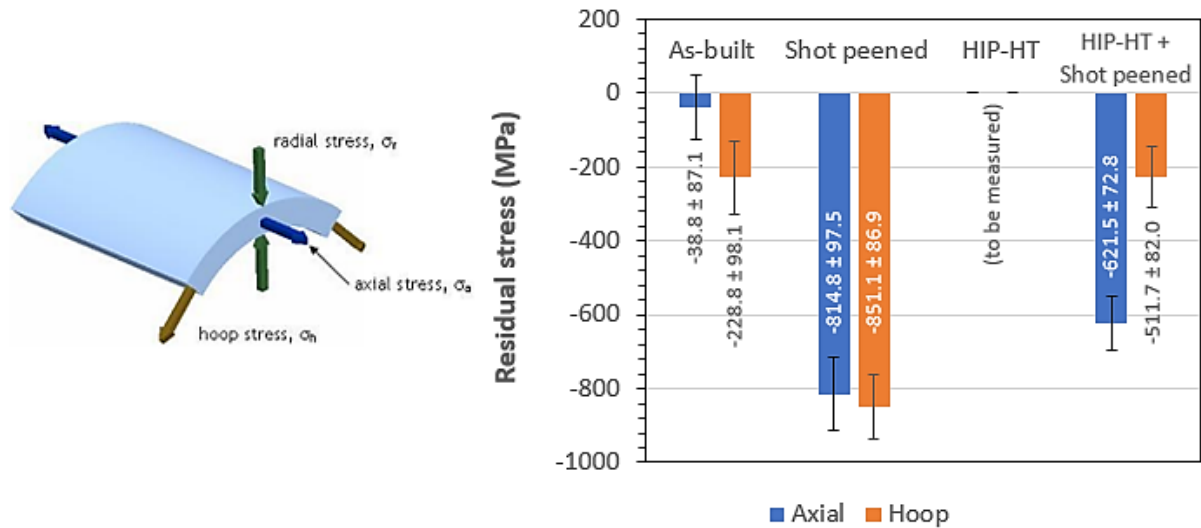
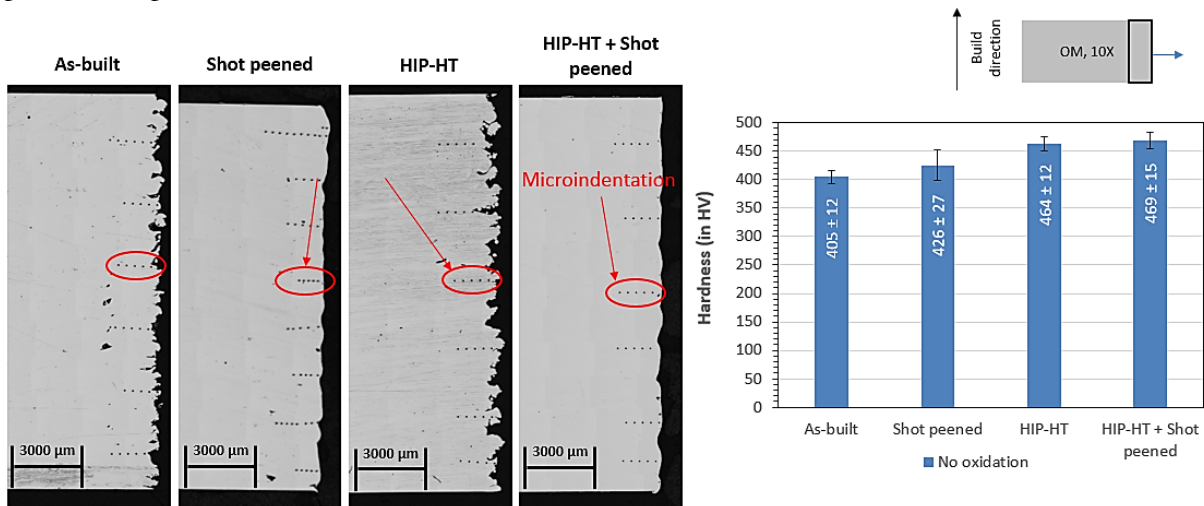


Figure 6.14: Schematic depicting the direction of axial and hoop stresses along with their corresponding measurements.

6.8. Hardness

It is seen that both shot peening and HIP-HT increases the hardness of the material. This can be seen in Figure 6.15 along with the micro-indentation marks. More standard deviation with a uniform mean value is observed in the microhardness versus distance plot after shot peening (see Figure 6.16). Anomaly in microhardness uniformity at 200 and 600 μm for as-shot peened and HIP-HT + shot peened samples respectively can be an effect of neighboring porosity. The error bar for non-shot peened samples is marked in red color for reference.



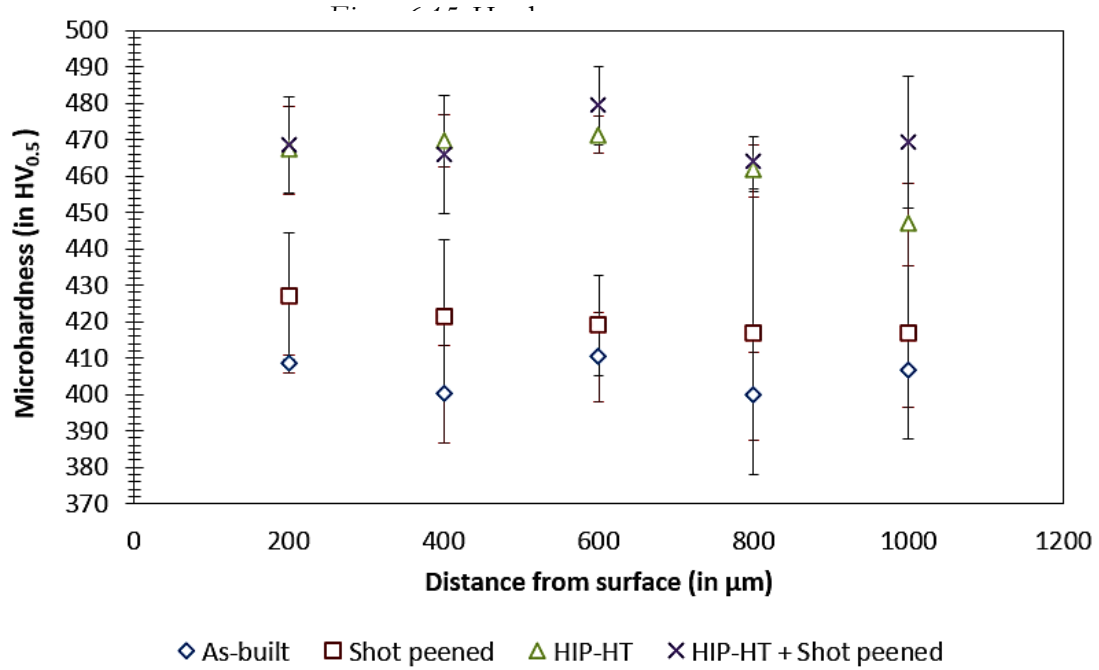


Figure 6.16: Change in hardness with respect to the distance from the surface.

6.9. Corrosion exposure results

6.9.1. Oxide layer

Both shot peening and HIP-HT reduced the oxide layer thickness (*see Figure 6.18*) for the same duration of exposure and temperature. It is seen from that shot peening on as-built sample had a greater influence on oxide layer thickness at 650 than at 800°C, and vice-versa for shot peening on HIP-HT sample. Influence of HIP-HT on oxide layer thickness is nearly the same for both the temperatures. Shot peening appears to make the oxide layer uniform for both the samples with more uniformity for as-built than HIP-HT sample at lower temperatures and vice-versa at higher temperatures. Both as-built and HIP-HT samples appear to be non-uniform with as-built having significantly higher non-uniformity at both the temperatures. All the samples under exposure at 800°C have a considerably higher oxide layer thickness than at 650°C.

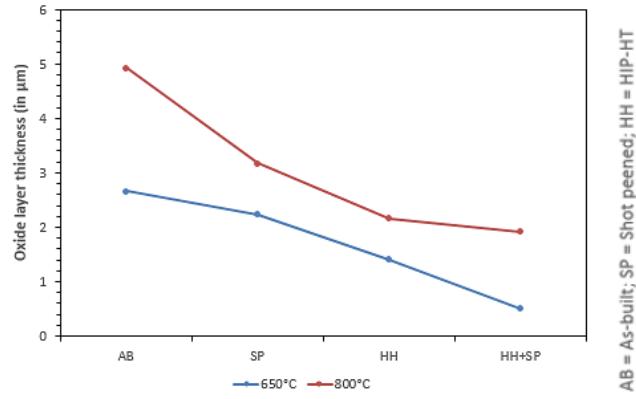


Figure 6.17: Trend in oxide growth according to post-processing.

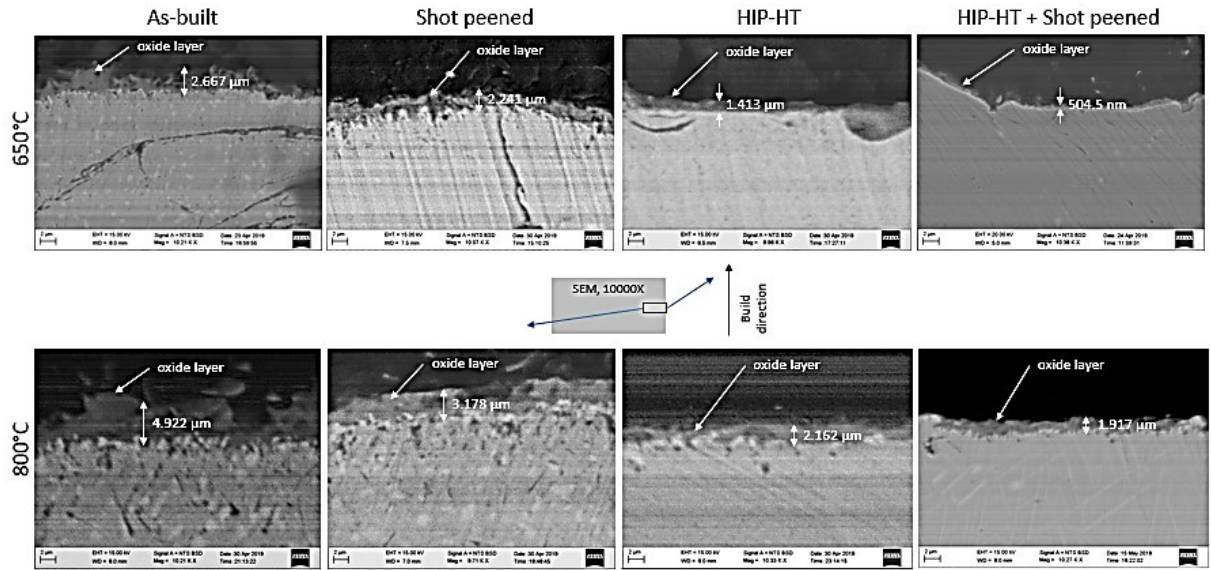


Figure 6.18: Oxide layer thicknesses formed on the samples with different post-treatment.

6.9.2. Weight gain

Shot peening, as well as HIP-HT, showed a reduction in weight gain for both with and without considering the weight of the crucible at both the temperatures for 96 h and 168 h (see Figures 6.19, 6.20, 6.22, and 6.23). However, it is seen that HIP-HT sample of 336 h exposure at 800°C, after shot peening showed more weight gain than before (see Figures 6.21 and 6.24). Weight gain for all the

samples followed a parabolic trend (see Figures 6.25 and 6.26) with HIP-HT + shot peened sample being as an exception, which cannot be characterized as any of the known trends.

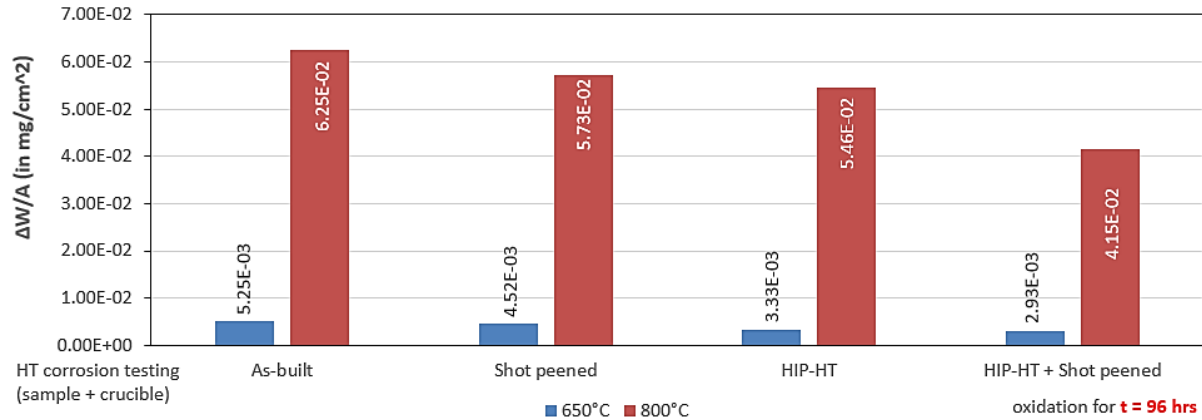


Figure 6.19: Weight gain of sample + crucible for 96 h exposure test.

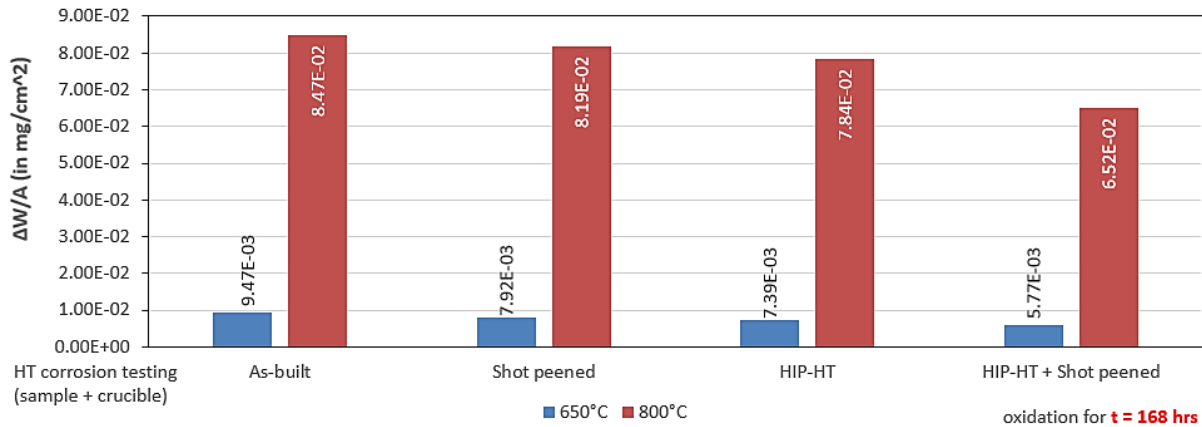


Figure 6.20: Weight gain of sample + crucible for 168 h exposure test.

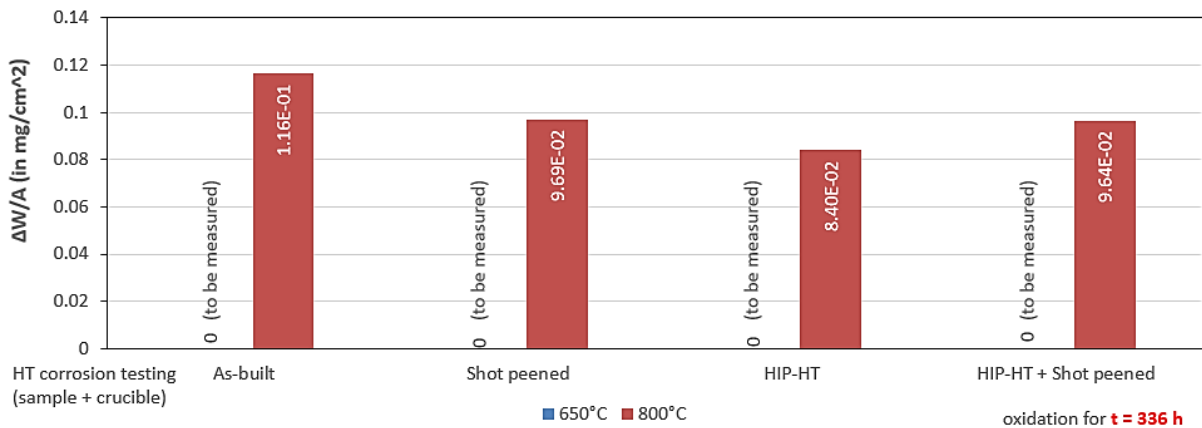


Figure 6.21: Weight gain of sample + crucible for 336 h exposure test.

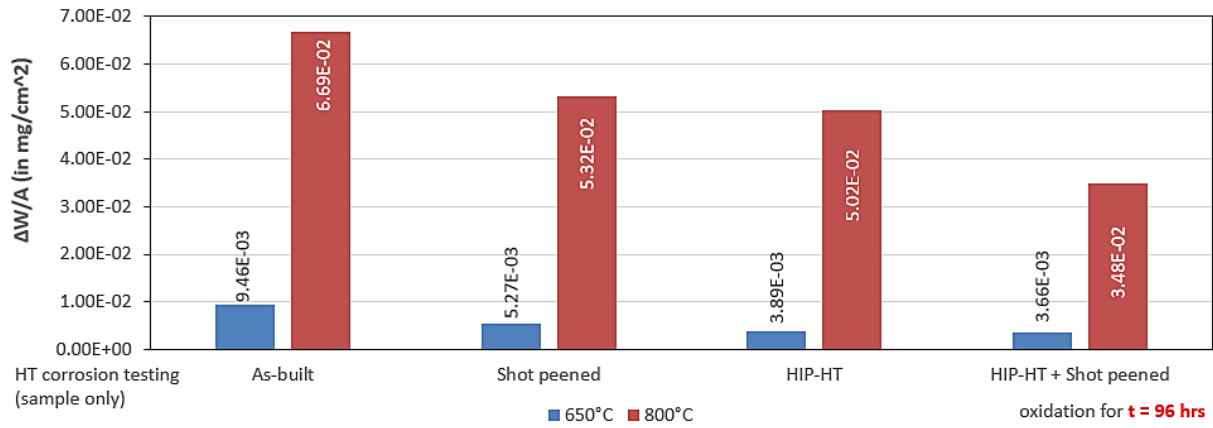


Figure 6.22: Weight gain of sample for 96 h exposure test.

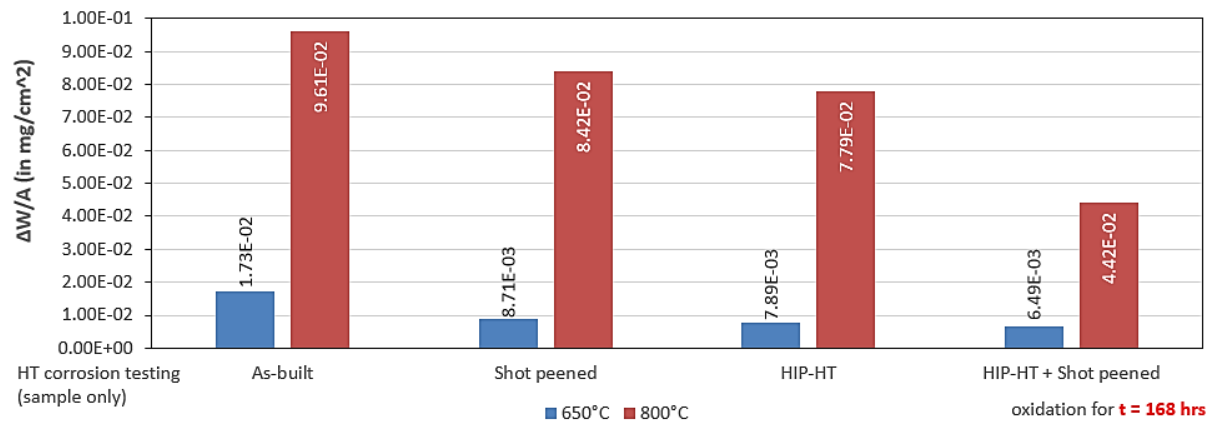


Figure 6.23: Weight gain of sample for 168 h exposure test.

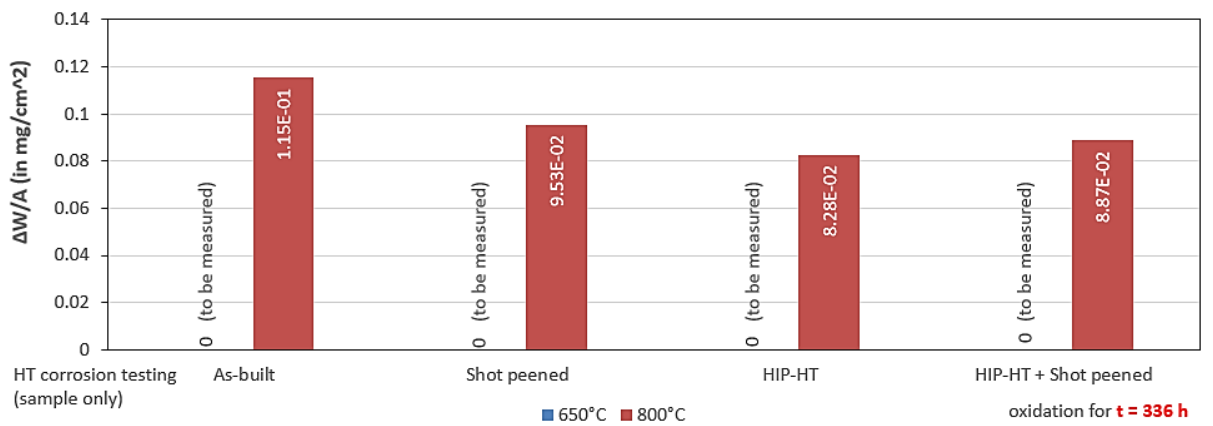


Figure 6.24: Weight gain of sample for 336 h exposure test.

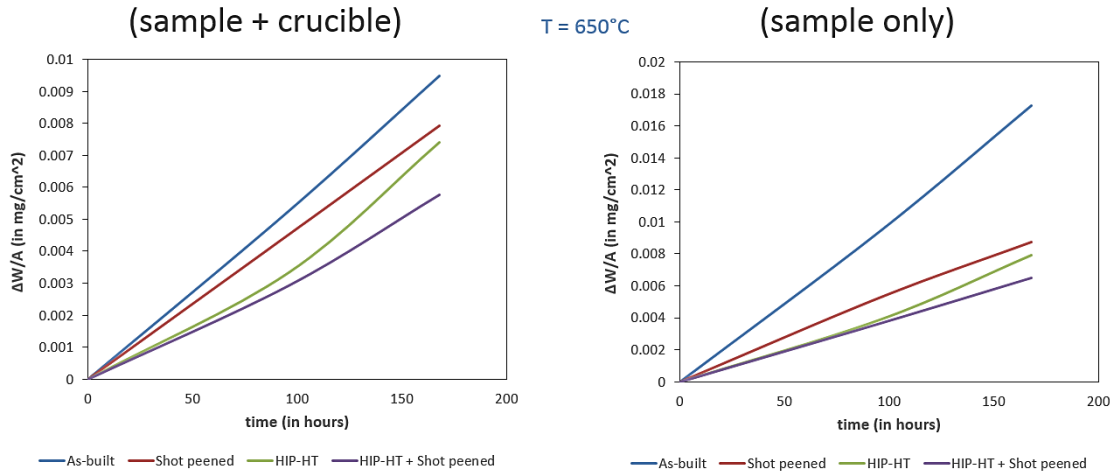


Figure 6.25: Trend in weight gain at 650 °C.

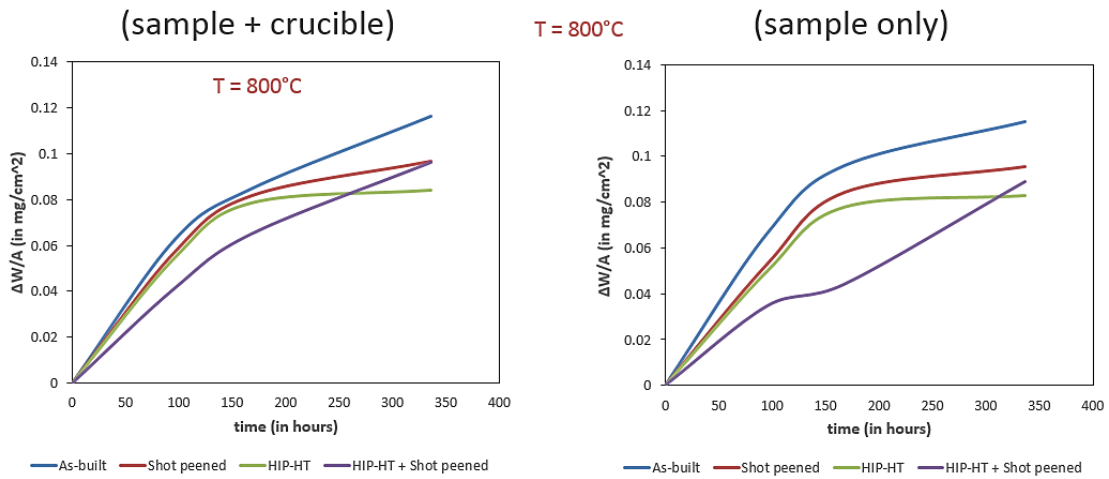


Figure 6.26: Trend in the weight gain at 800 °C.

6.9.3. Energy dispersive X-ray spectroscopy (EDS) analysis

Elemental distribution of O, Cr, Ni, Al, Fe, Ti and Nb at the oxide layer along with nearby regions at both 600 and 800°C has been provided below. Oxygen is present only at the surface before and after shot peening on the as-built sample, with other elements except for Al having redistribution of concentrations after shot peening at 800°C. More Al is seen at the surface after shot peening, and both the samples do not have uniform Al distribution at 800°C. However, at 650°C, all the elements except O tend to have a uniform distribution with O having a higher concentration at the surface after shot peening (*see Figures 6.27 and Figure 6.28*). Redistribution of Nb is observed after shot peening the HIP-HT sample. O is seen to be concentrated only at the surface in both the samples. Al has more concentration at the surface in HIP-HT sample, which becomes more homogenized after shot peening. All other elements are distributed uniformly for both the samples. Same changes were observed at both the temperatures (*see Figures 6.29 and 6.30*). Similar trends were observed as the surface mapping for line mapping with small variations of

different elements according to the uniformity of the oxide layer as can be seen from *Figures 6.31, 6.32, 6.33 and 6.34.*

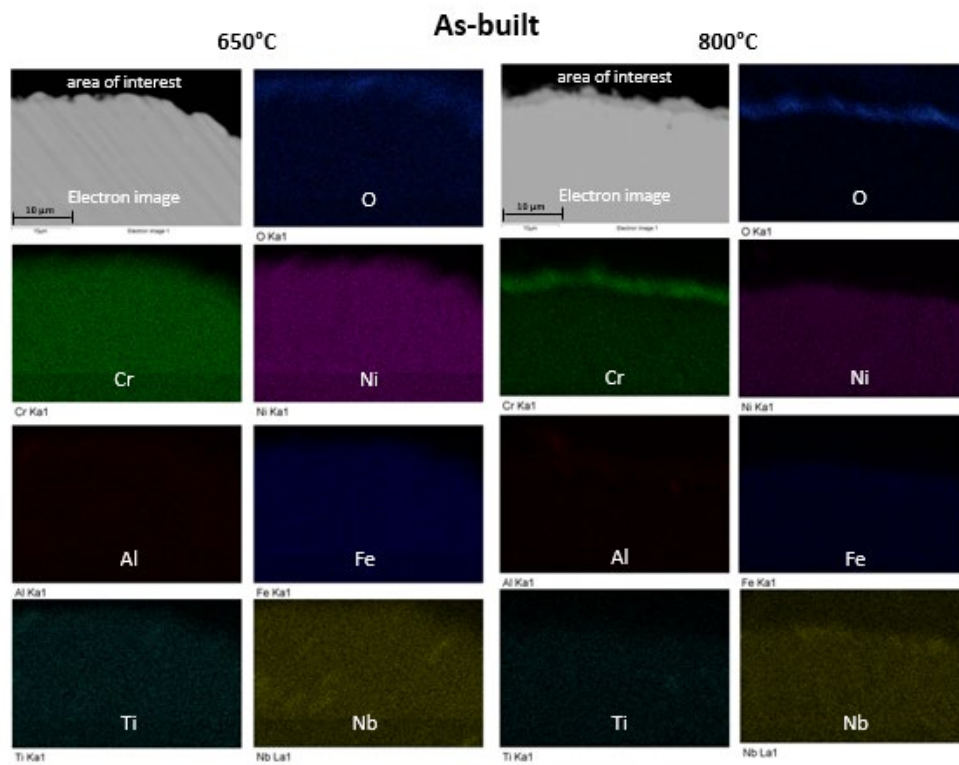


Figure 6.27: Surface elemental distribution for the as-built sample.

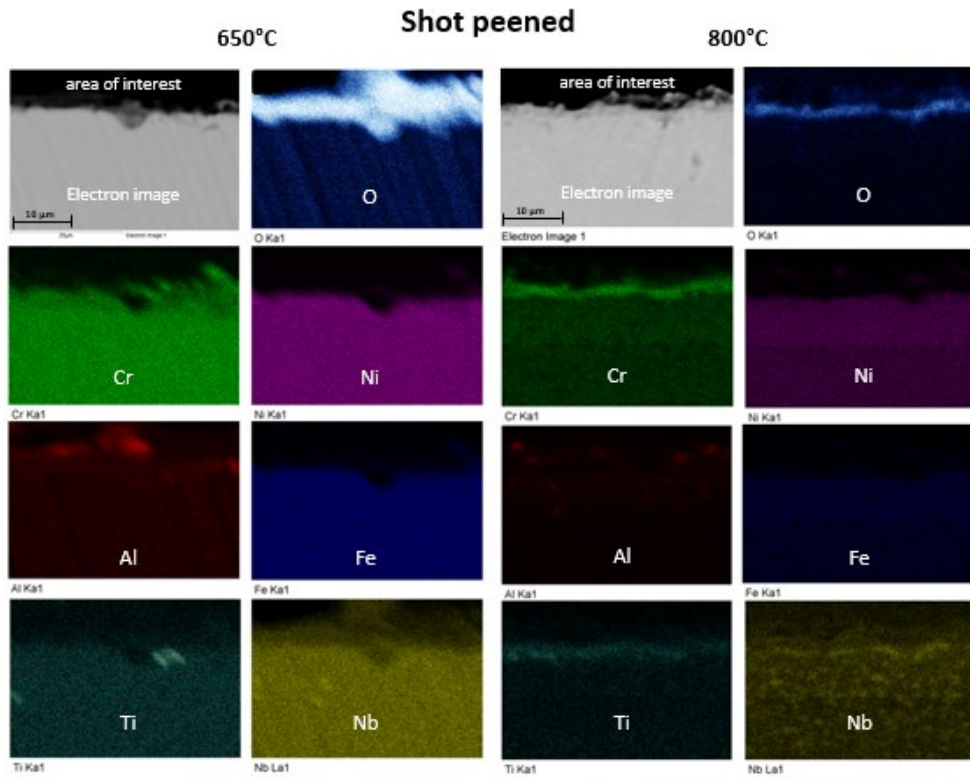


Figure 6.28: Surface elemental distribution for the shot peened sample.

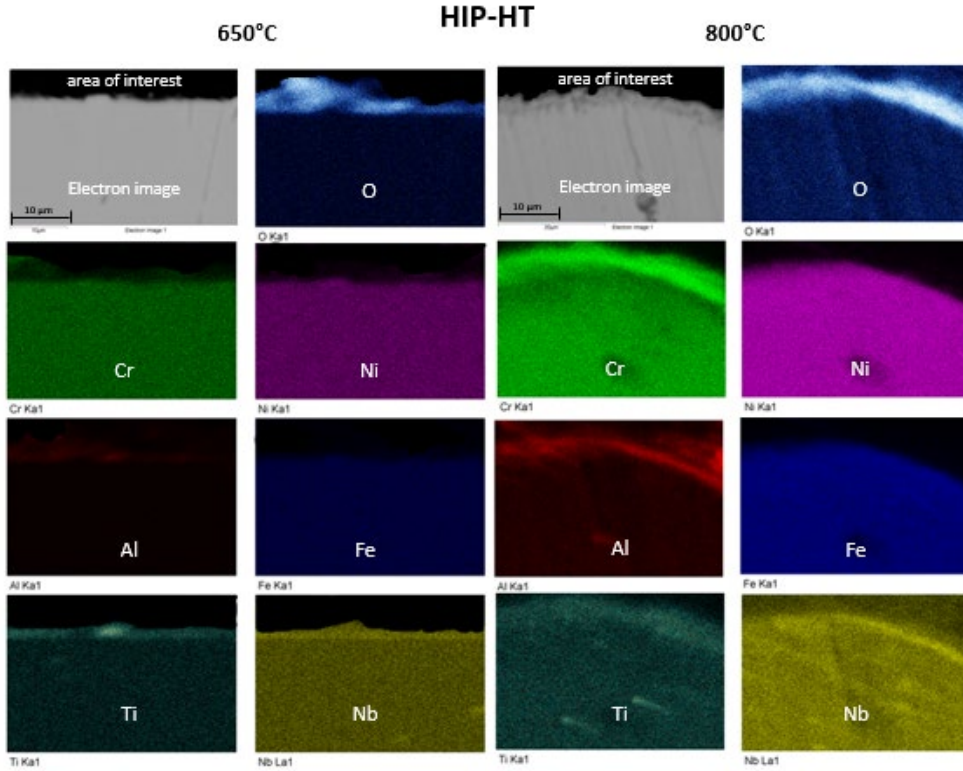


Figure 6.29: Surface elemental distribution for the HIP-HT sample.

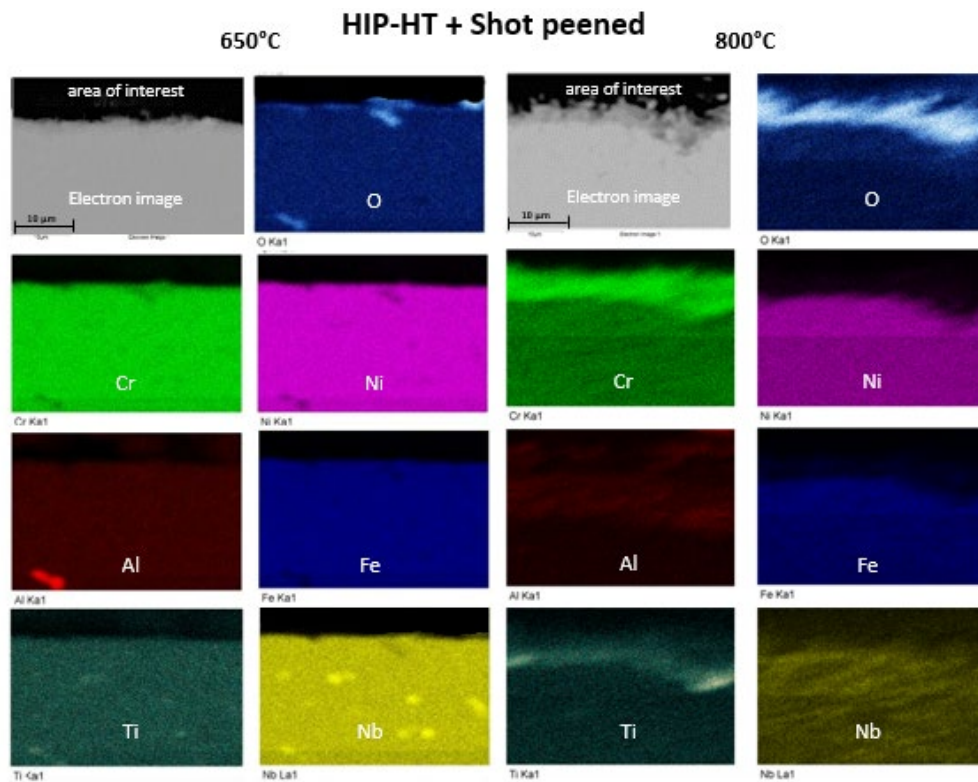


Figure 6.30: Surface elemental distribution for the HIP-HT + shot peened sample.

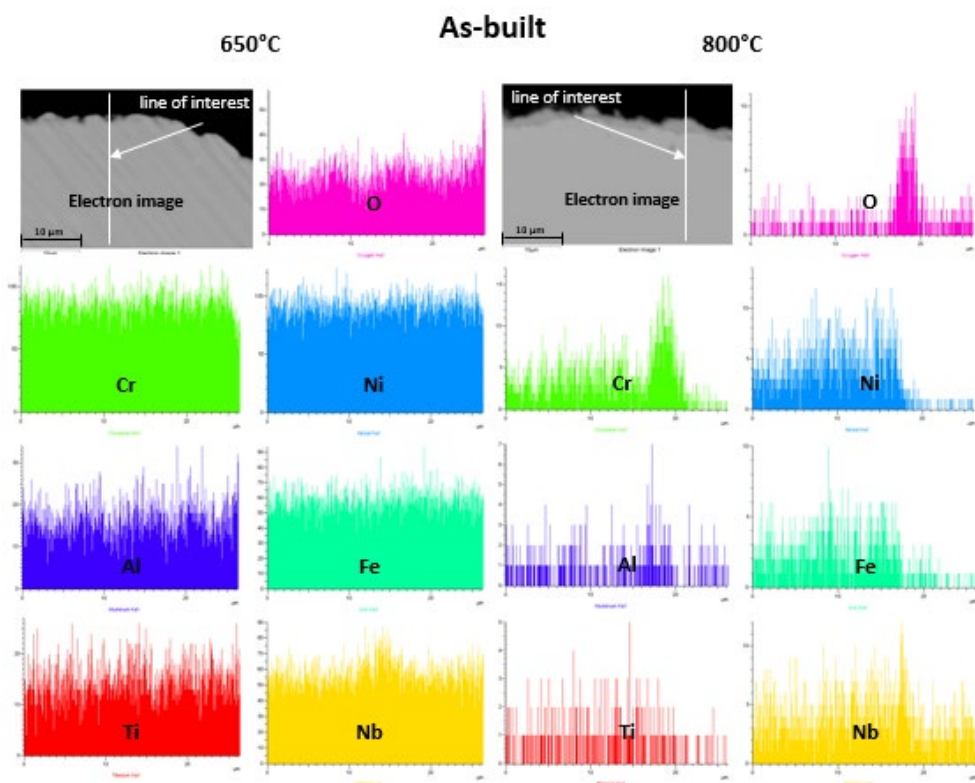


Figure 6.31: Line elemental distribution for the as-built sample.

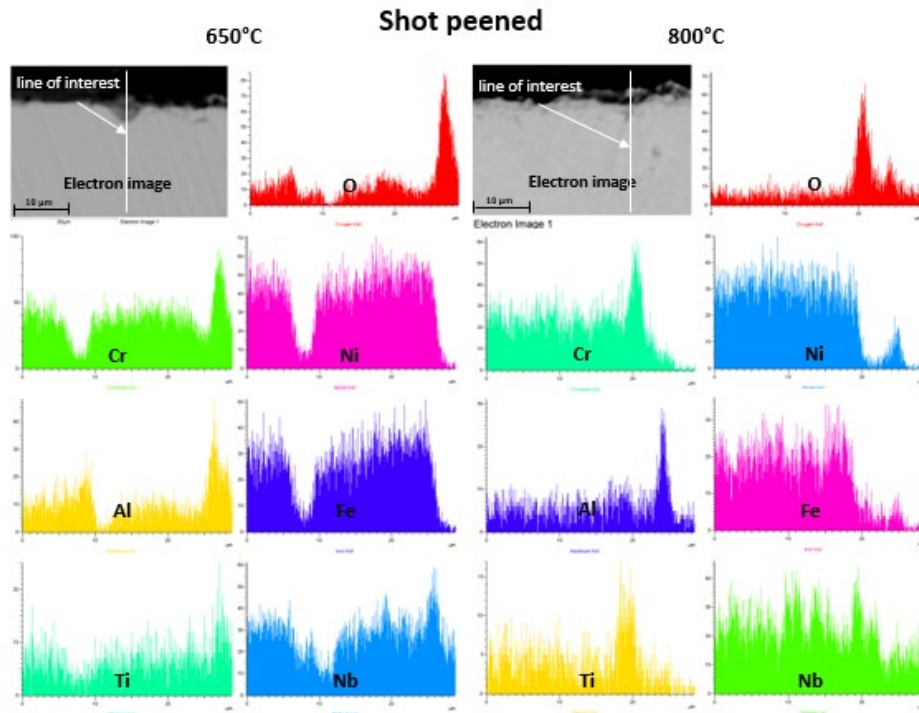


Figure 6.32: Line elemental distribution for the shot peened sample.

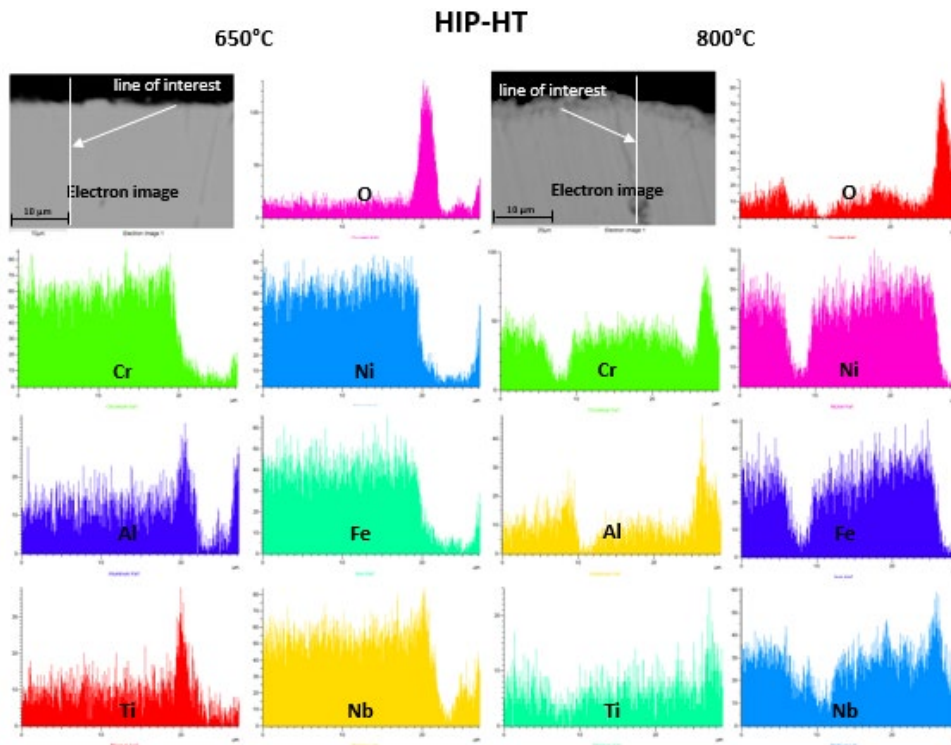


Figure 6.33: Line elemental distribution for the HIP-HT sample.

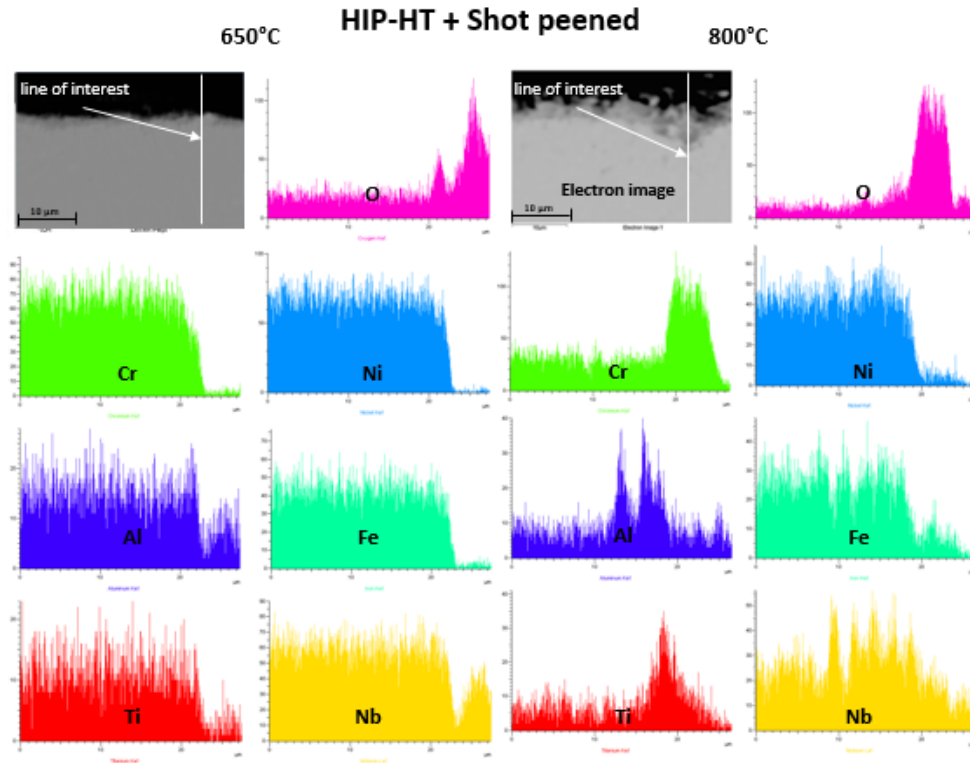


Figure 6.34: Line elemental distribution for the HIP-HT + shot peened sample.

6.9.4. Elemental point analysis

HIP-HT samples seem to have the highest corrosion resistance, as it can be seen from *Figure 6.35* that Cr has the least concentration on the oxide layer. It means that there is the least exploitation of Cr dissolved in the material, which enables the protective nature of the oxide (*refer section 4.2*). A similar trend is observed for Al and Ti as well at 800°C (*see Figure 6.35*), which also contributes to corrosion resistance, as they are more stable elements than Cr as seen from *Ellingham's diagram* (*see Figure 4.2*), however present in much lower concentrations (*see table 3.1*). However, Ti and Al concentrations vary (*see Figure 6.35*) after HIP-HT at 650°C. Lowest Nb concentrations are observed (*see Figure 6.35*) on the oxide layer in as-built and HIP-HT at 650 and 800°C respectively, meaning that strengthening the effect of HIP-HT comes to play at a higher operating temperatures. The same is true for shot peening, whose effect is observed to reduce after HIP-HT at higher temperature. Nb metal in spite of providing fatigue strength specifically at higher temperatures, one of the reasons behind using it as an alloying element in small quantity is because of its weight. The opposite trend of Nb is observed in both Fe and Ni (*see Figure 6.35*), meaning that both shot peening and HIP-HT increases the Fe and Ni depletion zones at high temperatures, with shot peening being worthwhile after HIP-HT. However, both Fe and Ni are selected for withstanding mechanical stresses rather than thermal stresses, and it is fine for them to exhibit this concentration characteristic on the oxide layer. It can be seen from *Figure 6.35* that oxygen has a high affinity towards the HIP-HT material at low temperature, which reduces drastically after increasing the temperature. Shot peening is observed to have increased the affinity of HIP-HT sample at higher temperatures and does not have a significant effect on as-built. Quantization of

elements at internal and external oxide layers separately was not possible, as it was not possible to distinguish between them by viewing at the cross-section.

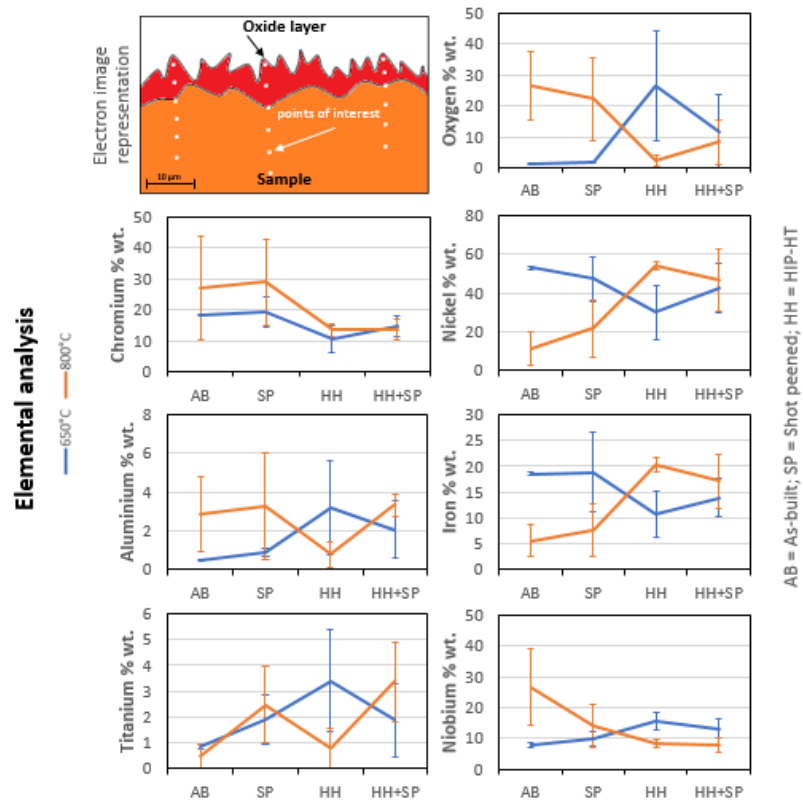


Figure 6.35: Variation in concentrations of individual elements for all samples.

7. Conclusions

Shot peening increased corrosion resistance by grain refinement, but HIP-HT reduced the corrosion resistance by grain enlargement. Shot peening on the as-built sample had no considerable effect on the Nb homogeneity. HIP-HT reduced the homogeneity of Nb, which then increased after shot peening. Shot peening increased intergranular δ . Shot peening minimized surface connected defects by continuous impact hammering while HIP-HT minimized bulk defects. At high temperatures, shot peening in both the samples caused needle-like oxide particles on the surface along with oval disk-shaped oxide particles, which was found alone in the samples without shot peening. Shot peening decreased the surface roughness both in as-built and HIP-HT samples by about ~ 32 to 34% and $\sim 20\%$, respectively. On the other hand, HIP-HT increased the surface roughness, which can be explained by the formation of new products (like oxides) at the surface once the sample was exposed to high temperature/pressure. Combined shot peening and HIP-HT had the highest surface roughness. Shot peening caused the chromia to plunge through the surface outward. HIP-HT created more surface irregularities, leading to the formation of distinctively higher oxide concentrations at the grain boundaries. The as-built and HIP-HT samples had only NiO or NiCr_2O_4 at the surface with later having a higher concentration, whereas the shot peened sample had only chromia and the HIP-HT + shot peened sample had both the oxides at the surface. Shot peening increased compressive stresses in the as-built sample of about 2100% axially and $\sim 372\%$ radially (hoop stress). Tensile residual stresses induced at low temperature did not completely cancel out the compressive residual stresses induced at high temperature due to atmospheric interaction. Shot peening also caused re-distribution of residual stresses on the surface, which does not vary as a whole from contour one towards two. Highest hardness resulted by combining both shot peening and HIP-HT. Standard deviations in the residual stress measurement (in both axial and radial directions) for the as-built and shot peened samples were nearly the same unlike that observed from hardness measurement. Shot peening after HIP-HT had a lower effect on both porosity and hardness compared to the as-shot peened sample. The as-built and HIP-HT samples, after shot peening, formed more protective oxide layers than others at low and high temperatures respectively. The as-built sample followed by the HIP-HT sample had the least protective oxide layers. Considering the corrosion resistance, the HIP-HT sample before and after shot peening had the most protective oxide layer (nearly to the same extent) at both the temperatures. All the samples at both the temperatures exhibited a slow-growing oxide layer over long durations with the oxides attaining stability earlier at a lower temperature, with HIP-HT + shot peened sample as an exception. Shot peening caused more surface concentration of O whereas, HIP-HT with more O diffusion into the bulk in spite of lesser oxide layer thickness.

References

- [1] Francis Froes and Rodney Boyer, *Additive Manufacturing for the Aerospace Industry*. Elsevier, 2019.
- [2] Jeff Dahl, *Federal Aviation Administration Handbook*. United States Department of Transportation.
- [3] Shirsat U.M. and Patil A.A., “Study of Failure Analysis of Gas Turbine Blade,” *IOSR Journal of Engineering*, vol. 2878–8719, pp. 37–33.
- [4] D. J. Young, *High Temperature Oxidation and Corrosion of Metals*. Elsevier, 2008.
- [5] William D. Callister, *Materials Science and Engineering*, 9th Edition SI Version. New York: John Wiley & Sons Inc, 2014.
- [6] Andreas Gebhardt and Jan-Steffen Hötter, *Additive Manufacturing: 3D Printing for Prototyping and Manufacturing*. Munich: Carl Hanser Verlag GmbH & Co. KG., 2016.
- [7] S. Uran, B. Veal, M. Grimsditch, J. Pearson, and A. Berger, “Effect of Surface Roughness on Oxidation: Changes in Scale Thickness, Composition, and Residual Stress,” *Oxidation of Metals*, vol. 54, no. 1, pp. 73–85, Aug. 2000.
- [8] D. Pradhan, G. S. Mahobia, K. Chattopadhyay, and V. Singh, “Effect of surface roughness on corrosion behavior of the superalloy IN718 in simulated marine environment,” *Journal of Alloys and Compounds*, vol. 740, pp. 250–263, Apr. 2018.
- [9] C. Sanz, V. G. Navas, O. Gonzalo, and G. Vansteenkiste, “Study of surface integrity of rapid manufacturing parts after different thermal and finishing treatments,” *Procedia Engineering*, vol. 19, pp. 294–299, Jan. 2011.
- [10] C. Sanz and V. García Navas, “Structural integrity of direct metal laser sintered parts subjected to thermal and finishing treatments,” *Journal of Materials Processing Technology*, vol. 213, no. 12, pp. 2126–2136, Dec. 2013.
- [11] W. Sames, “Additive Manufacturing of Inconel 718 using Electron Beam Melting: Processing, Post-Processing, & Mechanical Properties,” Thesis, 2015.
- [12] P. Karimi Neghlani, “Electron beam melting of Alloy 718 : Influence of process parameters on the microstructure,” 2018.

- [13] E. O. Hall, "The Deformation and Ageing of Mild Steel: III Discussion of Results," *Proc. Phys. Soc. B*, vol. 64, no. 9, pp. 747–753, Sep. 1951.
- [14] Petch N. J., "The Cleavage of Polycrystals," *Journal of Iron and Steel Institute*, vol. 174, pp. 25–28, 1953.
- [15] K. D. Ralston, N. Birbilis, and C. H. J. Davies, "Revealing the relationship between grain size and corrosion rate of metals," *Scripta Materialia*, vol. 63, no. 12, pp. 1201–1204, Dec. 2010.
- [16] P. Karimi, E. Sadeghi, D. Deng, H. Gruber, J. Andersson, and P. Nylén, "Influence of build layout and orientation on microstructural characteristics of electron beam melted Alloy 718," *Int J Adv Manuf Technol*, vol. 99, no. 9, pp. 2903–2913, Dec. 2018.
- [17] A. T. Polonsky, M. P. Echlin, W. C. Lenthe, R. R. Dehoff, M. M. Kirka, and T. M. Pollock, "Defects and 3D structural inhomogeneity in electron beam additively manufactured Inconel 718," *Materials Characterization*, vol. 143, pp. 171–181, Sep. 2018.
- [18] A. Strondl, M. Palm, J. Gnauk, and G. Frommeyer, "Microstructure and mechanical properties of nickel based superalloy IN718 produced by rapid prototyping with electron beam melting (EBM)," *Materials Science and Technology*, vol. 27, no. 5, pp. 876–883, May 2011.
- [19] C. Li, Z. Y. Liu, X. Y. Fang, and Y. B. Guo, "Residual Stress in Metal Additive Manufacturing," *Procedia CIRP*, vol. 71, pp. 348–353, Jan. 2018.
- [20] A. Townsend, N. Senin, L. Blunt, R. K. Leach, and J. S. Taylor, "Surface texture metrology for metal additive manufacturing: a review," *Precision Engineering*, vol. 46, pp. 34–47, Oct. 2016.
- [21] Srivatsan T.S. and Sudarshan T.S., *Additive Manufacturing : Innovations, Advances, and Applications*. Boca Raton: CRC Press, 2016.
- [22] K. Zaleski, A. Skoczylas, and M. Brzozowska, "THE EFFECT OF THE CONDITIONS OF SHOT PEENING THE INCONEL 718 NICKEL ALLOY ON THE GEOMETRICAL STRUCTURE OF THE SURFACE," *Adv. Sci. Technol. Res. J.*, vol. 11, no. 2, pp. 205–211, Jun. 2017.
- [23] S. Tammas-Williams, P. J. Withers, I. Todd, and P. B. Prangnell, "Porosity regrowth during heat treatment of hot isostatically pressed additively manufactured titanium components," *Scripta Materialia*, vol. 122, pp. 72–76, Sep. 2016.
- [24] J. Damon, S. Dietrich, F. Vollert, J. Gibmeier, and V. Schulze, "Process dependent porosity and the influence of shot peening on porosity morphology regarding selective laser melted AlSi10Mg parts," *Additive Manufacturing*, vol. 20, pp. 77–89, Mar. 2018.

- [25] A. Sandá, V. García Navas, and O. Gonzalo, "Surface state of Inconel 718 ultrasonic shot peened: Effect of processing time, material and quantity of shot balls and distance from radiating surface to sample," *Materials & Design*, vol. 32, no. 4, pp. 2213–2220, Apr. 2011.
- [26] H. H. Hooshyar, *High Temperature Corrosion of Stainless Steels in Low Oxygen Activity Environments -The effect of H₂ and H₂O*. 2016.
- [27] S. W. Guan and W. W. Smeltzer, "Oxygen solubility and a criterion for the transition from internal to external oxidation of ternary alloys," *Oxid Met*, vol. 42, no. 5, pp. 375–391, Dec. 1994.
- [28] A. S. Khanna, *Introduction to High Temperature Oxidation and Corrosion*. ASM International, 2002.
- [29] A. Chauhan, "Deformation and damage mechanisms of ODS steels under high-temperature cyclic loading," 2018.
- [30] ASTM E384-11e1, "Test Method for Knoop and Vickers Hardness of Materials," ASTM International.